UNIVERSITÀ DEGLI STUDI DI NAPOLI

FEDERICO II

DIPARTIMENTO DI INGEGNERIA INDUSTRIALE

Dottorato di Ricerca in Ingegneria Aerospaziale, Navale e della Qualità

Hydrodynamic Performance of Additive Manufacturing Marine Propellers

Gabriele Staiano

Tutor

Prof. Ing. Massimo Martorelli

Prof. Ing. Claudio Pensa

Prof. Ing. Antonio Gloria

Coordinator

Prof. Ing. Luigi de Luca

XXVIII Ciclo

Hydrodynamic Performance of Additive Manufacturing Marine Propellers

gabriele.staiano@unina.it

Department of Industrial Engineering, University of Naples Federico II, P.le V. Tecchio n. 80, 80125 Naples (ITALY)

Acknowledgements

The author acknowledges the support received by MBDA s.p.a. Italy and CNR IPCB (Istituto per i Polimeri, Compositi e Biomateriali), who provided the 3D print of aluminium alloy propeller and some important tests, data and information that have been very useful in carrying out this study and INSEAN to kindly provide with the propeller E779a data.

ABSTRACT

In recent years, a new generation of Additive Manufacturing (AM) techniques has rapidly become available to the public, due to the expiration of some AM patents and to open-source movements, which allowed significant cost reductions.

The aim of this study was to investigate the possibility to use Additive Manufacturing (AM) techniques in the field of naval propulsion, in particular in the fabrication of propellers in model scale, for experimental test, where the manufacturing process was remained almost unchanged in the last 50 years.

The naval contextualization responds to need for naval experimental laboratories (Towing Tank and Cavitation Tunnel) for which the high costs are an important limitation for both basic research and for industrial testing.

A further scope of applicability of the study is the realization of specialized design of custom propeller for fast boats (typically small) for which, the high cost of production, in relation to the commercial value of the product, has frequently a limitation.

Emphasis was placed to printing process parameters and physical and mechanical characterization of materials used to provide reliable and accurate data as references for developers, designers and researchers.

The used procedures, were specialized in relation to the intrinsic requirements of the propellers and of the chemical and physical characteristics of the materials.

Most marine propellers are made of metallic material such as bronze or steel. The advantages of replacing metal with a polymeric and composite materials are that the latter is lighter and corrosion-resistant. AM process has the potential to dramatically reduce the time and cost required realizing functional metal parts. In addition, the process can fabricate complex internal features not feasible using existing manufacturing processes and allow to fabricate customized propeller.

The case study propeller INSEAN E779a, considered in the literature an adequate benchmark, was taken into account.

It was fabricated by Direct Metal Laser Sintering (DMLS) EOS M280 in AlSi10Mg metal powder and by an open-source Fused Deposition Modeling (FDM) 3D printer, Prusa Mendel I3 in Acrylonitrile-Butadiene-Styrene (ABS), and UltraT polymeric material.

The study of printing parameters and the accurate physical-chemical and mechanical tests on the thermoplastic materials were taken into account, performing Differential Scanning Calorimetry (DSC) analysis, Thermogravimetric Analysis (TGA) and Flexural Tests, and have allowed to optimize the printing process conditions.

The evaluation of the printed propellers was carried out by combining their morphological data with the comparison of their performance in respect to the benchmark.

A Reverse Engineering system, Faro Articulated Arm Coordinate Measuring Machines (AACMM) CAM2, was used to get the point clouds of each propeller. Using the iterative closest point algorithm of Geomagic Control software of 3D Systems, the point cloud of each propeller was aligned with the CAD nominal model.

In such a way the analysis of the deviations was carried out.

Atomic Force Microscopy (AFM) test allowed to assess the morphological features and surface roughness of the printed propellers.

Towing tank open water propeller tests were carried out and hydrodynamic performance comparison analysis between printed propellers and benchmark, in terms of torque and drag, was analysed.

Also, having carried out the measures to 1 kHz sampling frequency, were evaluated the effects, on the hydrodynamic performance of the propellers, of the residual polar asymmetries due to shrinkage associated to AM process.

Computational Fluid Dynamic (CFD) analysis were performed to determine the loads acting on the propeller which were used in the experimental bending test on printed propellers.

The results, show differences in respect of the thrust generated and of the torque absorbed by the printed propellers, compared to benchmark, as function of the advance coefficient J, of the morphological characteristics and of the materials used. However, the final analysis showed that the substantial adequacy of the AM propellers realized, for most of the studies carried out in Towing Tank.

This is due both to the reduced deviations from the nominal model, that to verified constancy of performance offered by each prototype.

CONTENTS

FIGURE INDEX

TABLE INDEX

INTRODUCTION

The ASTM International Committee F42 on AM technologies defines AM as the "process of joining materials to make objects from three-dimensional (3D) model data, usually layer by layer, as opposed to subtractive manufacturing methodologies [1].

Common to AM technologies is the use of a computer, 3D modelling software (CAD), machine equipment and layering material.

Once a CAD model is produced, the model data, usually converted in stereolithography (STL) format, are first decomposed into a series of 2D, finitely thick cross sections, which are then fed into an AM machine that lays downs or adds successive layers of liquid, powder, sheet material or other, in a layer-upon-layer fashion to fabricate a 3D object in metallic, plastic, ceramic, composite, or biological materials.

AM processes have many advantages over traditional manufacturing processes such as a cost-effective and time-efficient way to produce low-volume, customized products with complicated geometries and advanced material properties and functionality, material waste is greatly reduced.

From the first patent registered on March 11, 1986 from Charles W. Hull, up to the present day, AM has evolved into a different kinds of processes, including Stereolithography (SLA), Fused Deposition Modeling (FDM), Laminated Object Manufacturing (LOM), Selective Laser Sintering (SLS), Selective Laser Melting (SLM), Direct Metal Deposition (DMD), Laser Metal Deposition (LMD), inkjet printing, and others.

The AM techniques, for several advantages, previously mentioned, may be used to the construction of marine propellers, whose production process has remained virtually unchanged over the past decades, to responds the need of naval experimental laboratories (Towing Tank and Cavitation Tunnel) for which the high costs are an important limitation for both basic research and industrial testing and for the realization of specialized design of custom propeller for fast boats (typically small) to overcome the limitation due to the high cost of production, in relation to the commercial value of the product.

The aim of this study was to analyse and compare two AM techniques and to assess the adequacy of these to the construction of marine propellers, for towing tank open water propeller test, combining their morphological data with the comparison of their hydrodynamic performance in respect to a benchmark propeller.

In particular, a DMLS process was used to print an aluminium alloy propeller and a FDM process was used to print propellers in two different types of thermoplastic materials.
The employed procedures were specialized according to the intrinsic requirements of the propellers and of the chemical and physical characteristics of the materials.
The study of printing parameters and the accurate physical-chemical and mechanical tests on the thermoplastic materials have allowed to optimize the process conditions.

1. THE CASE STUDY INSEAN E779a

The case study propeller INSEAN E779a, considered in the literature an adequate benchmark, was took into account.

The E779a (Figure 1) is a four blade right-handed propeller, Wageningen modified type, with a diameter of 227.27 mm, a forward rake angle of 4° 3", blade skew and rake are small, and pitch ratio is almost constant along radius (pitch/diameter = 1.1).

The propeller was originally designed in 1959 for a twin-screw ferry but unfortunately no full-scale data are available.

In the 60's the model propeller was chosen as reference propeller model of the Italian Navy Cavitation Tunnel (C.E.I.M.M.). Details of propeller geometry can be found in [2], [3], [4] and [5].

A bronze model of propeller was used for experimental work and during the VIRTUE project the actual geometry of the propeller blade was measured and an IGES file created.

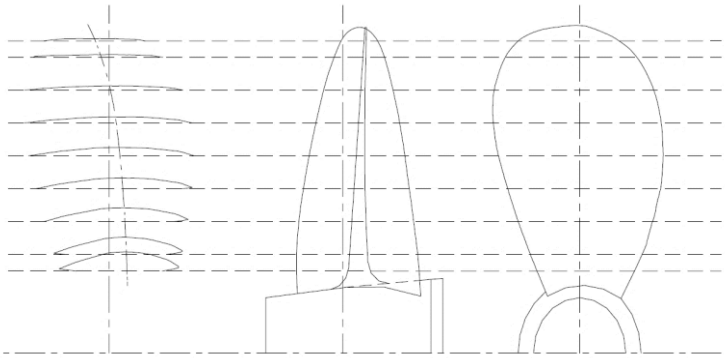

Figure 1: The INSEAN E779a propeller

Performance characteristics in terms of dimensionless thrust K_T and torque K_Q coefficients, depending on the advance coefficients J were provided by the INSEAN (Figure 2) and reported in ANNEX I.

According to ITTC (International Towing Tank Conference) recommended procedures [6] and [7], the dimensionless K_T, K_Q and J coefficient were defined as:

$$K_T = \frac{T}{\rho n^2 D^4}\ ; \tag{1.1}$$

$$K_Q = \frac{Q}{\rho n^2 D^5} \tag{1.2}$$

and

$$J = \frac{V}{nD} \tag{1.3}$$

where T (N) and Q (N · m) were the propeller thrust and torque, n (rps) was the propeller rotational speed, D (m) the propeller diameter and ρ (kg/m^3) was water density.

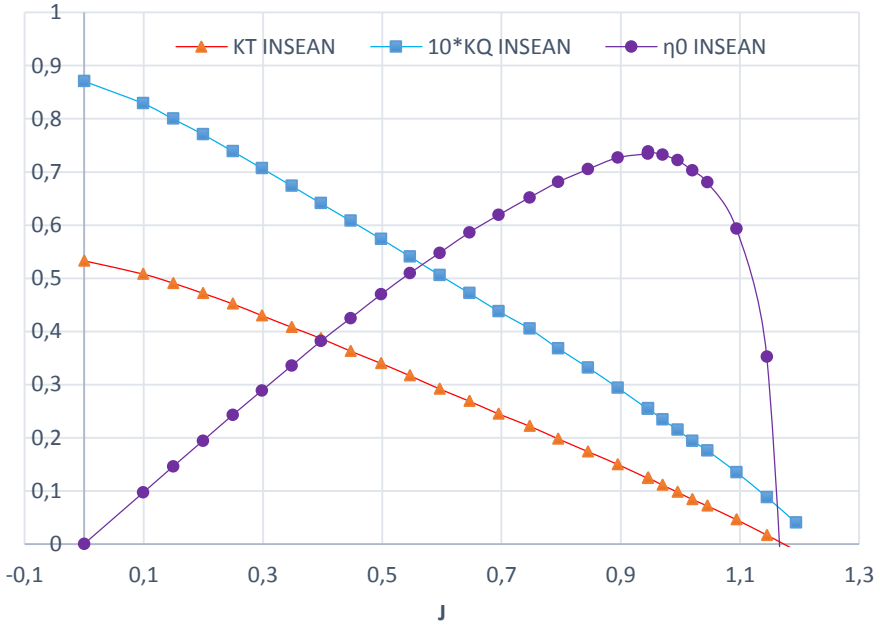

Figure 2: E779a propeller performance characteristics

Starting from the mathematical description of one blade (IGES), new solid geometrical model was prepared in Rhinoceros V5 CAD software, of Robert McNeel, and used in the current work (Figure 3).

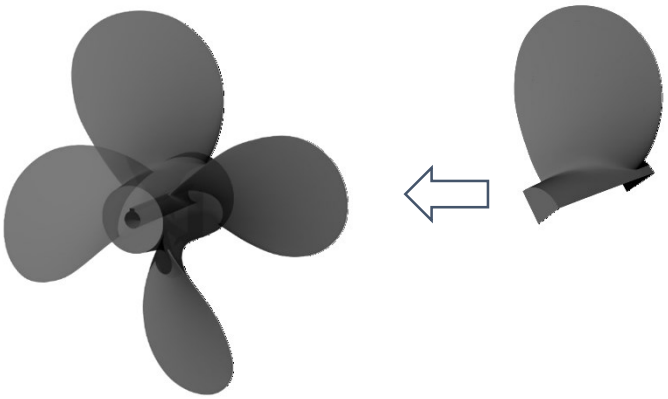

Figure 3: E779a propeller CAD model

2. ANALYSIS OF PRINTING PROCESS PARAMETERS

Among the different AM technologies currently available, in the present study two techniques were considered: Fusion Deposition Modeling (FDM) to print two propellers in two different thermoplastic materials and a Direct Metal Laser Sintering (DMLS), that allowed to manufacture the propeller in aluminium alloy.
In order to optimize the printing process conditions, studies about the effects of the main printing process parameters, with respect to the produced parts, were carried out.

2.1. AM techniques

AM processes include countless technologies that fabricate three-dimensional parts layer upon layer starting from a CAD model.
AM processes can be categorized following two different criteria [8]: the first one is based on the kind of technology used, while the second one is based on the kind of material that can be processed.
With respect to the physical state of raw material, AM processes are classified into four principal classes, based, respectively, on liquid, filament/paste, powder or solid sheet.
AM processes may also be classified depending on the class of raw materials, such as polymers, metals, ceramics, composites and biological materials.
According to ASTM F42 Committee AM processes were classified into seven categories shown in Table 1.

Process Category	*Technology*	*Part Material*
Vat photopolymerisation	*SLA*	*UV curable resins* *Waxes* *Ceramics*
Material jetting	*MJM*	*UV curable resins* *Waxes*
Binder jetting	*3DP*	*Polymer* *Metal* *Composites*
Material extrusion	*FDM*	*Thermoplastic* *Waxes*
Sheet lamination	*LOM*	*Paper* *Metal* *Thermoplastic*
	UAM	*Metal*
Directed energy deposition	*LMD*	*Metal*
	LENS	*Metal*
Powder bed fusion	*SLS*	*Thermoplastic* *Metal*
	DMLS	*Metal*
	SLM	*Metal*
	EBM	*Metal*
	SHS	*Thermoplastic*

Table 1: AM Processes categories

An overview on different AM categories and their main characteristic, is described [8].

- Vat photopolymerisation (Stereolithography, SLA) uses a vat of liquid photopolymer resin, out of which the model is constructed layer by layer using an ultraviolet (UV) light to harden the resin, where required, whilst a platform moves the object being made downwards after each new layer is polymerized.

- Material jetting (Multi Jet Modeling, MJM) jetting material onto a build platform, using a Drop On Demand (DOD) approach, where it solidifies and the model is built layer by layer.

  Material is deposited from a nozzle which moves horizontally across the build platform in a similar method to a two dimensional ink jet printer.

  The material layers are then polymerized using ultraviolet (UV) light.
- Binder jetting (3D Printing, 3DP) involves building a model in a container filled were, for each layer, a roller spreads and compress a measured amount of material powder, such as either starch or plaster material, over the building platform.

  For each layer, a multichannel jetting head applies a calibrated quantity of liquid adhesive to bond the particles of material together and form the two-dimensional cross section of the object.

  Upon application of the binder, a new layer is swept over the prior one, with the application of more binder, and this process is repeated until the model is complete.
- Material extrusion (Fusion Deposition Modeling, FDM) involves feeding a thermoplastic filament (typical thickness 1.75÷3 mm) into a heated extrusion nozzle that melts and deposits the material moving, by convention, in the X and Y axes, to form the horizontal plane on a table that moves, on the Z axis, to build up layer by layer the model.
- Sheet lamination processes include Laminated Object Manufacturing (LOM) and Ultrasonic Additive Manufacturing (UAM).
  - LOM use paper material and adhesive, basing on a layer by layer approach and, for this reason, are often used for aesthetic and visual models and are not suitable for structural use.

    The process uses a cross hatching method, during the printing process, to allow for easy removal post build.
  - UAM process uses sheets, or ribbons, of metal, which are bound together by ultrasonic welding involving low temperature and allowing to create internal geometries.

    The UAM requires, often during the welding process, additional CNC (Computer Numerical Control) machining and removal of the unbound metal.

    As the metal is not melted, the process requires relatively low energy and different materials can be bonded.

- Directed Energy Deposition (DED), that includes Laser Metal Deposition (LMD) and Laser Engineered Net Shaping (LENS) processes, is a more complex printing process commonly used to repair or add additional material to existing components. Typically machine, consists of a nozzle mounted on a multi axis arm, which deposits melted material onto the specified surface, where it solidifies.

  The principle of process is similar to material extrusion, but, otherwise, the nozzle is not fixed to a specific axis and can move in multiple directions.

  The material, which can be deposited from any angle due to 4 and 5 axis machines, is melted upon deposition with a laser or electron beam. The process is typically used with metals but polymers and ceramics can be used in the form of either powder or wire.

  - Laser Metal Deposition (LMD) built up the part, layer by layer, using a laser beam to form a melt pool on a metallic substrate, into which powder is fed from a nozzle.

    The powder melts to form a deposit that is bonded to the substrate and both the laser and nozzle are manipulated using a gantry system or robotic arm.
  - Laser Engineered Net Shaping (LENS) fabricates three-dimensional metal component deposing, sequentially, consecutive layers using a metal powder injected into a molten pool created by a focused, high-powered laser beam.

    Simultaneously, the substrate on which the deposition is occurring is scanned under the beam/powder interaction zone to fabricate the desired cross-sectional geometry.
- Powder Bed Fusion processes include the following printing techniques: Direct Metal Laser Sintering (DMLS), Electron Beam Melting (EBM), Selective Heat Sintering (SHS), Selective Laser Melting (SLM) and Selective Laser Sintering (SLS).

  The fundamental difference between these technologies is the mean that they use to expose the powder (electron beam, laser beam or thermal print-head).

  - Direct Metal Laser Sintering (DMLS) is the same layer by layer process as Selective Laser Sintering (SLS) but the first one sintering metals materials, while, the second one sintering polymeric materials.

- Electron Beam Melting (EBM), usually used to build functional parts in metals and alloys materials, require a vacuum ambient. All powder bed based processes involve the spreading of the powder material over previous layers, by means of different mechanisms, including a roller or a blade.
  A hopper or a reservoir below of aside the bed provides fresh material supply.
- In Selective Heat Sintering (SHS), layers are added with a roller in between fusion of layers and the platform lowers the model accordingly but differs from other processes, since it uses a heated thermal print head to fuse powder material together.

2.2. Fused Deposition Modeling (FDM)

Based on previous works [9], [10] and [11], the analysis and the optimal setup of the printing process parameters, for FDM process have been identified using a DOE approach.
Until a few years ago, manufacturing high-quality physical prototypes or products required very expensive AM systems and investments in tooling and sophisticated specific software. This posed a barrier to the widespread deployment of such systems, now used by big companies, research institutes or innovative start-ups.
3DP is rapidly becoming available to the masses thanks to recent developments driving down the cost and complexity of the machines.
The current expansion of the new generation 3D printers has benefited from the expired 3DP patents for fused deposition modeling, where objects are built up layer by layer with extruded melted plastic) and from the open-source movement (for both software and hardware—Arduino hardware).
Available on the web, the cost of these new open-source 3D printers ranges from 400 to 2000 €.
Today, new low-cost AM systems allow for the production of parts also in metal [12], [13] and [14].
3DP is considered as the production technology of the future, enabling "the third industrial revolution" [15], [16] and [17].

In recent times, the increasing interest of industry in RP processes and their application is also evident from the development of standards through ASTM International and the International Organization for Standardization (ISO) [18] and [19].

One of the most famous and successful open-source projects of 3D printer development is known as the RepRap (replicating rapid prototyper) Project [20].

It was developed in 2005 by Adrian Bowyer with the University of Bath (UK).

The aim was to develop a 3D printer capable of replicating a significant number of its own structural components.

The remaining parts were selected from standard engineering materials and components available cheaply worldwide. This project is original and unique.

Currently, for these systems there is a significant lack of scientific data concerning the appropriate selection of process parameters in order to improve accuracy and to save time.

For the previous study, an open-source RepRap Prusa-Mendel I2 3D printer (0.35mm nozzle diameter) and a 2.85mm PLA biodegradable material were used with the aim to evaluate the impact on system accuracy of important process parameters such as layer thickness, deposition speed, and flow-rate, as well as to improve the knowledge about optimal settings.

First, the 3D printer was calibrated. The calibration phase of a RepRap 3D printers, in fact, is a fundamental phase. It allows the motors to move the correct distance each time they move the build platform or the extruder, so as to obtain objects with the same dimensional characteristics, also if they are fabricated by different RepRap of the same type (for this research Prusa-Mendel I2).

The calibration was performed using a dial indicator with magnetic base, Mitutoyo 2046-08 (Mitutoyo, Japan) with an accuracy of ±μm. MARLIN (open-source) was used as the firmware software and CURA (open-source) as the software which converts STL files into G-code files able to command and control the system in order to obtain the final 3D object printed.

The methodology employed in this study consists of sequential procedures aimed to produce and measure benchmarking parts made using the RepRap Prusa-Mendel I2. Figure 4 shows the general work flow adopted.

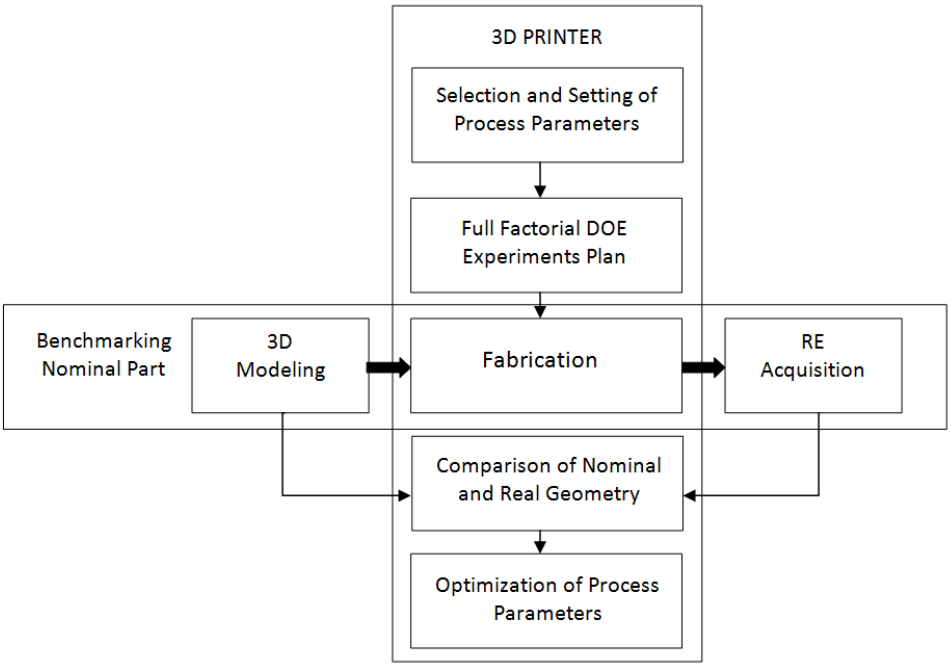

Figure 4: Logical work-flow for the comparison of benchmarking nominal and real parts fabricated following a full factorial design

Various studies on the design of benchmarking parts for evaluating the accuracy and repeatability of RP processes are available, see for example, Kruth [21], Lart [22], Iuliano et al. [23], Juster and Childs [24] and [25], Shellabear [26], Mahesh et al. [27], and Hopkinson and Sercombe [28].

Unfortunately, however, none of the proposed parts comprehensively included all the features necessary to establish the desired accuracy/repeatability related parameters.

In 2012, Fahad and Hopkinson [29] proposed a new benchmarking part (Figure 5 on the left) that includes elementary shapes representative of all the main features useful for evaluating accuracy and repeatability (cube, cylindrical hole, sphere, solid cylinder, hollow cylinder, cone, angled surfaces) in a very compact manner.

Ten features are replicated three times to evaluate variability.

This benchmarking part was taken into account for this study but to allow the fabrication in the same printing and laser scanner acquisition, the 10 features were placed side by side as shown in Figure 5 on the right.

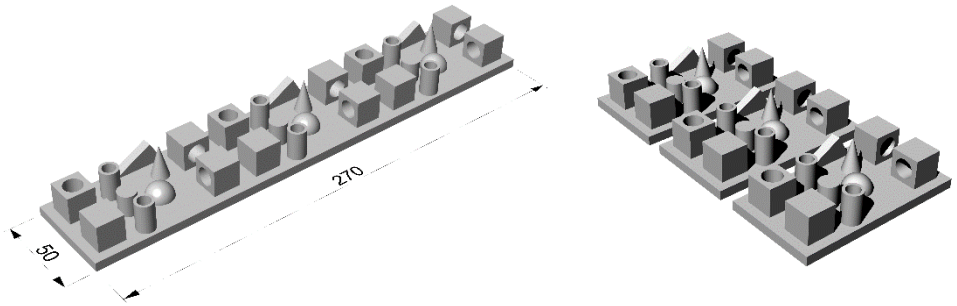

Figure 5: Benchmarking part [29] with three replications of 10 main features used in the Study

The study of the factors involved in the experimentation is a crucial task.
It was done mainly through focus group with RepRap experts and on the basis of literature review related to consolidated RP processes.
Layer thickness (A), deposition speed (B), and flow rate (C) were adopted as control factors. Table 2 shows other process parameters that were held constant throughout the experimentation.
The control factors can be set in all the main slicing software (CURA, KISSLICER, SLIC3R, SIMPLIFY3D) and they are defined as:

- Layer thickness (mm) is the thickness of each slice of the part building and it is the step along the vertical axis taken before extruding a new layer atop the previous one. In Refs. [30] and [31], it is known that with a lower layer height a better accuracy of the part is obtained.
- Deposition speed (mm/s) is the speed with which the hotend moves; with a lower deposition speed it is obtained a better accuracy of the part but an increase in the fabrication time.

- Flow rate (%) is the flow of material that is extruded from the hotend and is expressed as a percentage of the number of revolutions that the motor of the extruder has to do, to extrude 1mm of filament.

Constant factors	***Value***
Wall thickness (mm)	*0.7*
Bottom/top thickness (mm)	*0.6*
Fill density (%)	*20*
Bed temperature (°C)	*80*
Printing temperature (°C)	*200*

Table 2: Process parameters held constant throughout the experimentation

For each control factor, the range of variation was chosen considering that the aim of the study is to understand the main effects of process parameters on the accuracy.

For the layer thickness, considering that with a lower deposition speed it is obtained a better accuracy of the part, as mentioned above, the authors, in the predesign phase, carried out tests with a layer thickness value of 0.05 mm.

Therefore, for the layer thickness the minimum value chosen was 0.10 and it was increased in steps of 0.05 mm.

For the deposition speed, the range of typical values is 30–120 mm/s. Considering that with a lower deposition speed it is obtained a better accuracy of the part, as mentioned above, the authors, to ensure the best performance in term of accuracy, considered the minimum value of 30 mm/s and a maximum value of 80 mm/s.

For the flow rate, based on the experience of the RepRap experts the three values, 100%, 105%, and 110% were chosen.

All control factors and conditions set for the experimental treatments are listed in Table 3.

Factor	Level		
	-1	0	1
A - Layer thickness (mm)	0.10	0.15	20
B - Deposition speed (mm/s)	30	55	80
C - Flow rate %	100	105	110

Table 3: Control factors and their levels for the fabrication of the benchmarking parts

A full factorial design, with three factors at three levels (see ANNEX II), and three replications (Figure 5) was carried out to obtain 81 PLA prototype using Prusa-Mendel I2 [32], [33] and [34]. Each benchmarking part was acquired using a high resolution Laser Scanner, D700 Scanner—3Shape, Denmark to generate the cloud points.

The accuracy of this noncontact Reverse Engineering system is of ±20μm.

RE acquisition should be defined a noise factor adding a variation to the process.

For this study it has been considered as a constant factor, because all the parts are acquired by the same laser scanner and operator following the same procedure.

In this way the variation due to the acquisition is effectively smaller than variation due to process.

The 3D models obtained were then compared with the nominal CAD model, i.e., nominal benchmarking part.

Data processing was performed in GEOMAGIC software, using an iterative closest point algorithm [35], to minimize the distance between the clouds point and nominal CAD model.

The choice of alignment between point cloud and nominal CAD model should be a noise factor.

In this exploration study it has been considered as a constant factor, because all parts were aligned using the same procedure and the point clouds were checked by the same expert operator.

Two planes and one sphere were used to fit each point cloud to CAD model.

The YZ plane was obtained selecting two aligned sides of external cubes, the XY plane was obtained selecting the upper surface of the base and the sphere was obtained selecting the hemisphere.

These data allow to define the alignment procedure of each point cloud and the CAD model: two data plane lock five degree of freedom and the last one is locked by the datum sphere (Figure 6).

All sequences of three data (sphere, XY plane, and YZ plane) were evaluated to choose the optimal alignment.

In order to minimize deviation, the adopted alignment sequence was sphere - XY plane - YZ plane.

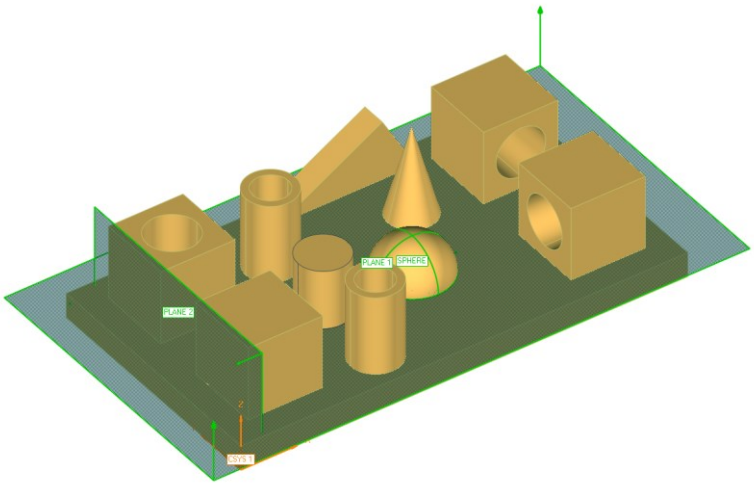

Figure 6: Alignment of the point clouds with the CAD model through the three datum

Starting from the results reported in ANNEX II, it can be highlighted that:

- Factor B is the most important factor with a CR equal to 34%.
- Factors A and C are equally important having the same CR equal to 22%.
- Interactions AC and AB show a cumulated CR equal to 16%, so it should be useful to take into account the simultaneous effect of both interactions even if each interaction seems to be not significant (see the ANOVA test in Table 22 of ANNEX II)
- Cumulated CR of factors A, B, C, AC, and AB is greater than 90% that is the Pareto ANOVA threshold [32] to take into account significant effects.

The main effect plot (Figure 7) shows that the choice of the levels -1 of factor A (0.10 mm), -1 of factor B (30 mm/s), and 0 of factor C (105%), is the optimal expected combination that maximizes the accuracy, i.e., minimizes RMS.

The interaction plots (Figure 8) show that the choice of the level -1 of factor A (0.10 mm) mitigates the accuracy loss when factor B is selected at level 0 (30 mm/s).

Furthermore, the same effect happens when factor A is at level -1 (0.10 mm) or level 0 (0.15 mm) and the factor C is selected at level 0 (105%) or level 1 (110%).

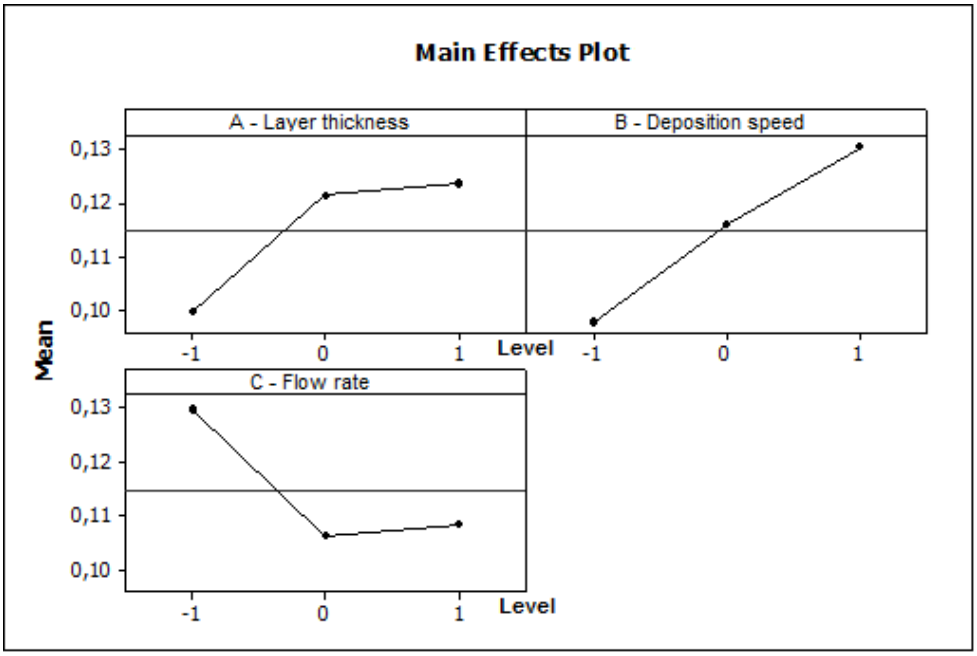

Figure 7: Main effects plot of the three process parameters (A,B,C) at three levels (-1,0,1) on the response RMS

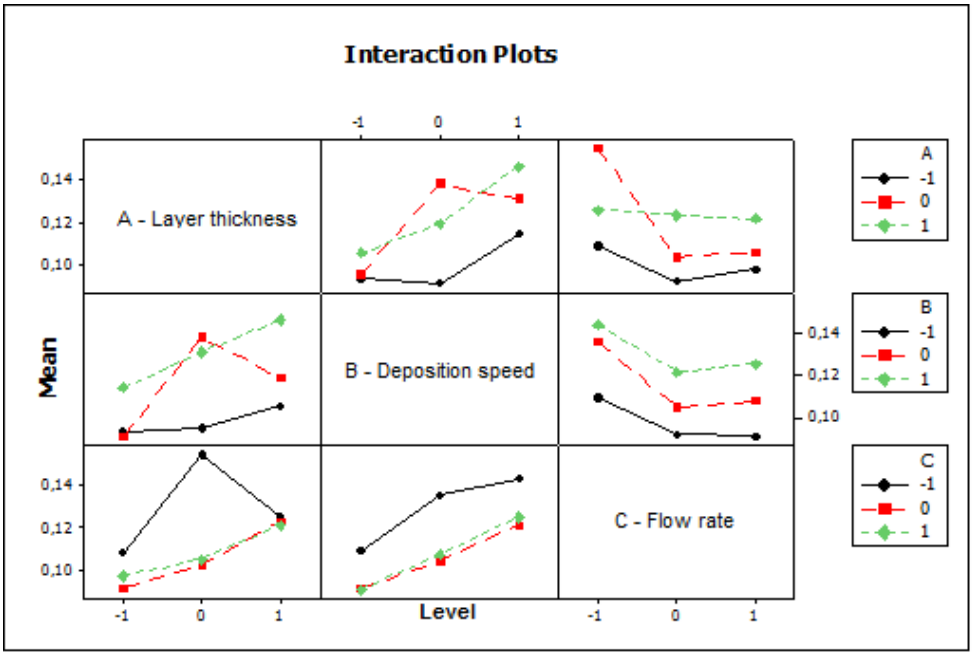

Figure 8: Interaction plots of the three process parameters (A,B,C) at three levels (-1,0,1) on the response RMS

It also can be settled out that:

- The lowest value of deposition speed (factor B), i.e., 30 mm/s, maximizes the accuracy. The expected result is in accordance with common sense.
- The lowest value of layer thickness (factor A), i.e., 0.10 mm, maximizes the accuracy. This value can be considered as an optimal value because previous tests, carried out considering layer thickness values less than 0.10mm (e.g., 0.05 mm), showed accuracy loss of the prototype.

  This result agrees with a "rule of thumb" that empirically suggest a value of layer thickness equal to one-fourth of the nozzle as optimal choice (in this test the diameter is 0.35 mm).
- The choice of level 1 (110%) is acceptable being the RMS differences very small if compared to the results of level 0. So the practical suggestion to increase the flow rate over the 100% is correct and the effects on the accuracy are robust, being the improvement obtained in a wide range (from 105% to 110%).

- The best prototype was n. 2. This result agrees with the expected optimal combination (-1,-1,0) and it suggests that the mean effect model well fits real data.
- The worst prototype was n. 13. It was obtained with the combination (0,0,-1). This result highlights a significant effect of interaction. It means that the mean effect model (i.e., the model without interactions) does not explain completely real data. This limit requires new experimental tests to improve model fitting and to better understand the interactions as source of variability.

Starting from these results, to give new practical insight about the choice of process parameters, the fabrication time is taken into account.

Table 4 shows the best and worst prototypes in terms of accuracy and fabrication time and some good compromise in terms of both responses.

The first practical suggestion is that maximum accuracy is not correlated to maximum fabrication time, being significant the effect of flow rate.

The second practical suggestion is that to save time, the layer thickness can be increased to the highest value. In this case, the time saving is about 50% and the loss in accuracy is approximately 25%.

The third practical suggestion is that if the accuracy is not critical (being acceptable till a mean value of 0.15) it is recommended to set both layer thickness and deposition speed to the highest value to obtain the minimum fabrication time.

In this case the interaction effect is meaningful, being this setting robust against flow rate variation.

Prototype	Factor			Mean rms [mm]	St.dev.	Time [min]
	A	B	C			
2	-1	-1	0	0.08	0.011	288
3	-1	-1	1	0.09	0.003	288
21	1	-1	1	0.10	0.004	148
20	1	-1	0	0.10	0.005	148
14	0	0	0	0.10	0.002	160
4	-1	0	-1	0.10	0.010	229
1	-1	-1	-1	0.11	0.015	288
26	1	1	0	0.14	0.005	115
27	1	1	1	0.15	0.010	115
25	1	1	-1	0.15	0.011	115
13	0	0	-1	0.20	0.072	160

Table 4: Control factors and their levels for the fabrication of the benchmarking parts

The final suggestion is to take care of level settings and to avoid neutral choice (see prototypes n. 14 and n. 26, that is the worst), being not true that *in medio stat virtus.*

2.3. Direct Metal Laser Sintering (DMLS)

Direct Metal Laser Sintering (DMLS) is a typical Additive Manufacturing (AM) process based on the layer by layer powder spreading and subsequent laser sintering [36].
Therefore, DMLS enables production of complex 3D shaped functional parts directly from metal powders.
Based on the experience of experts and on literature review, a number of variables introduced by the DMLS process, such as laser scan speed, layer thickness, support structures, and part

orientation that contribute to the final geometric tolerances and surface roughness and that affect the final quality of the part, have been taken into account.

The main causes of variability in the DMLS process and the relative impact in the final characteristics of the printed part, are reported and grouped in respect of raw materials, of model data preparation and setup of printing process in the Table 5,Table 6 and Table 7.

Materials behave differently during the sintering/melting process so it is necessary to customize exposure, recoating, and heating settings for each raw powder.

Obviously, within the same kind of raw material, properties of the individual powder batch that is loaded into the printer, have an effect on working conditions, energy input, part throughput and post-processing.

Anomalous values of these properties could generate variability within sintering/melting operations, hence in the final characteristics of the printed part.

Material properties that could enhance DMLS process variability are resumed in the Table 5, together with their common effects [37].

Material property	***Material property***
Particle size distribution	*Sinterability/meltability* *Packing efficiency* *Surface roughness*
Particle shape	*Packing efficiency*
Apparent / tap density	*Packing efficiency*
Melting point	*Indicator of energy requirements*
Strength of green part	*Facilitates part handling before thermal cycle (debinding, sintering, infiltration)*
Specific heat, thermal conductivity	*Heat transfer in powder bed*
Void fraction	*Residual porosity in printed parts*
Flowability	*Uniform spreading of powder layer*

Table 5: Sources of variability in DMLS processes due to the properties of materials

Proper data preparation is an important prerequisite for the correct implementation of ALM processes and to avoid a job failure or the poor quality of the produced parts.
Some of countless geometric and topological parameters that affect this phase are presented in Table 6.

Geometric / topological parameter	*Affected characteristic*
Part inclination (build angle)	*Mechanical properties* *Part accuracy* *Process speed*
Part positioning on the plate	*Mechanical properties* *Part accuracy* *Shrinkage/distortion*
Part orientation	*Mechanical properties* *Part accuracy* *Shrinkage/distortion*
Type and number of supports	*Mechanical properties* *Process speed* *Wasted material amount* *Surface roughness*
Z- height	*Process speed* *Part accuracy* *Surface roughness*
Layer thickness	*Mechanical properties* *Part accuracy* *Process speed*

Table 6: AM process variability due to geometrical and topological settings

Layer thickness, has a fundamental role in respect to the process speed and part accuracy. Generally, low levels of layer thickness result in better geometrical and mechanical properties of the sintered part.

However, a small layer thickness always involves increased build times.
In DMLS process, every protruding, or overhanging, surface needs to be fixed on the building platform and properly supported, in order to allow the layer-by-layer growth of the part.
This is achieved by means of fixation structures, called supports.
Supports require time and material to be created (as well as the part).
Moreover, after building they have to be removed from the platform and the part by sawing, wire-cutting or spark-erosion.
Before choosing the supporting strategy, it is important to analyse the part orientation and inclination according to specific criteria such as:

- z-height - larger z-height can reduce the amount of surfaces which have to be supported, but it increases build time and risk of supports collapse;
- maximum cross section – minimizing the exposure area per layer ensures the heat drain from exposure areas and reduces the internal stress, thus enhancing mechanical properties;
- growing direction – as well as for the part, preventing the growth of supports to run counter the powder spreading direction, results in reduced risk of lifting of a layer under the action of the re-coating blade, which can cause distortion and irregularities within the processed material, damage to the blade itself and interruption of printing process.
- build angle – Higher build angles lead to increased build times, but they are necessary to reduce internal stresses and improve part quality for some geometries.

When the part has been oriented, the operator can proceed to generate support structures, bearing in mind the countless critical issues in executing this step, such as removability, surface quality alteration and heat drain from the part.
The positioning on the building area also affects the final properties of parts, depending on the print volume isotropy characteristics of the used device.
During printing (sintering/melting) phase, variability can arise mainly to ambient conditions and exposure settings such as laser power, (that affects the amount of energy that can be delivered to the material) or hatching distance (that is the distance between the lines during the sintering of inner area, after the contour exposure, that affect the mechanical strength and also surface roughness of the DMLS prototypes).

Compliance with the ambient conditions is essential for a trouble-free process and for avoiding wear or degradation of the equipment, as shown in Table 7.

Geometric / topological parameter	***Affected characteristic***
High temperature in room	*Overload of the cooling system* *Inadequate cooling of the optical assemblies* *Formation of condensed water on cooled assemblies*
Low temperature in room	*Formation of condensed water on trim panels and housings*
High ambient moisture content in room	*Formation of condensed water on trim panels and housings*
Inadequate supply of inert gas	*Building process is interrupted*

Table 7: Sources of variability in AM processes due to ambient conditions

Open literature, focuses on the fundamentals of the laser sintering process and the evaluation of the materials produced by this method by looking at mechanical properties and microstructure have investigated the application of DMLS to actual component quality.
Some of these studies have quantified the surface roughness and the effect of process variables on the final part quality.
Simchi et al. [38] studied a simple iron-based DMLS part and reported surface roughness while Khaing et al. [39] reported roughness for a nickel–bronze–copper DMLS part evaluating, in addition the geometric tolerance of the test specimen.
Senthilkumaran et al. [40] and Song and Koenig [41] investigated the effect of various DMLS process parameters (laser scan speed, laser power, and hatching distance) on the surface roughness.
Delgado et al. [42] studied, in addition, the effect of build direction on surface roughness and dimensional tolerance for stainless steel DMLS parts.

Wong et al. [43] examine heat transfer and pressure loss through additively manufactured heat exchangers.

Calignano et al. [44] investigated the effect of various DMLS process parameters studying DMLS of AlSi10Mg powder through an experiment based on Taguchi approach in order to assess the influence of processing parameters (hatching distance, scan speed and laser power) on surface roughness.

It obtains that low scan speeds resulted to improve the top surface finish giving to the melt pools more time to flatten before solidification.

On the other side, a too low scan speed could increase the volume of liquid produced within the melt pool and balling phenomenon could arise.

With respect to laser power, higher values resulted in reducing the melt pool tendency to undergo balling by relieving surface tension variations.

However, if laser power is too high, material vaporization can occur and recoil pressures can disrupt the melt pool surface.

N. Read, et al. [45] investigate the influence of Selective Laser Melting (SLM) process parameters on the porosity development in AlSi10Mg was investigated by means of DOE approach, focusing on laser power, scan speed, scan spacing and island size.

Experimenters identified a low energy density region corresponding to a high porosity due to the lack of consolidation and a high energy density region (approximately over 60 J/mm^3) where other defects, such as keyhole formation (due to vaporization), have been observed within the material.

These information allow to evaluate and optimize the correct DMLS printing process conditions.

3. ANALYSIS OF AM MATERIALS USED

Concerning the materials used in the study, two type of thermoplastic polymers have been used to print the propellers trough the FDM process whereas a powder of aluminum alloy, AlSi10Mg, has been used to print the propeller in metal alloy by means of the DMLS process [46].

3.1. FDM filaments

The two thermoplastic polymers used to print the propellers trough the FDM process were provided by Zortrax S.A., Poland, under the trade name Z-ABS and Z-UltraT.
The main data relative bulk Z-ABS material [47] are shown in Table 8 while those relating the bulk Z-UltraT [48] are reported in Table 9.

Mechanical Properties	***Test Method***	***Value***
Young's Modulus	*DIN EN ISO 527-2 (ASTM D638)*	*1.80 GPa*
Tensile Strength	*DIN EN ISO 527-2 (ASTM D638)*	*38 MPa*
Tensile elongation	*DIN EN ISO 527-2 (ASTM D638)*	*17 %*
Rockwell R hardness	*PN-EN ISO 2039-1 (ASTM D785)*	*109*

Table 8: Main Z-ABS material data sheet

Mechanical Properties	*Test Method*	*Value*
Young's Modulus	*DIN EN ISO 527-2 (ASTM D638)*	*1.95 GPa*
Tensile Strength	*DIN EN ISO 527-2 (ASTM D638)*	*42 MPa*
Tensile elongation	*DIN EN ISO 527-2 (ASTM D638)*	*21 %*
Rockwell R hardness	*PN-EN ISO 2039-1 (ASTM D785)*	*110*

Table 9: Main Z-UltraT material data sheet

The materials were provided as filaments with a diameter of 1.75 mm in spool by the weight of 800 g.

3.2. Calorimetric analysis of thermoplastic materials

Differential Scanning Calorimetry (DSC) and thermogravimetric analysis (TGA) were carried out on the polymeric materials.

Specifically, DSC analysis was performed on Z-ABS and UltraT at 10°C/min, according to the ASTM D3417 [49] and ASTM D3418 [50].

This test method covers the determination of heat of fusion and heat of crystallization of polymers by differential scanning calorimetry.

It may be is applied to polymers in granular form or to any fabricated shape from which appropriate specimens can be cut.

This method consists of heating or cooling the material at a controlled rate in a specified purge gas at a controlled flow rate, then comparing the areas under the crystallization exotherm or fusion endotherm of the test material against the respective areas obtained by the similar treatment of a well-characterized standard.

Basically, DSC provides a rapid method for evaluating enthalpy changes accompanied by the first-order transitions of materials.

The heat of fusion, the heat of crystallization, and the effect of annealing may be generally evaluated in polymers that possess them.

Differential scanning calorimetry may be used to assist in identifying specific polymers, blends, and certain polymer additives which exhibit thermal transitions.

This test method is useful for both process control and specification acceptance, as well for research purpose.

Results from DSC analysis performed on Z-ABS and Z-UltraT have been reported in terms of heat flow-temperature curves (Figure 9 and Figure 10).

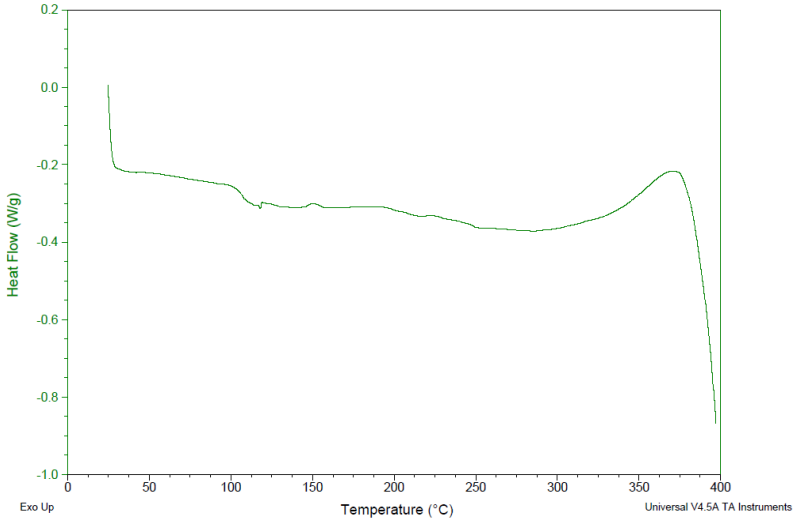

Figure 9: DSC analysis: typical curve of heat flow versus temperature for Z-ABS

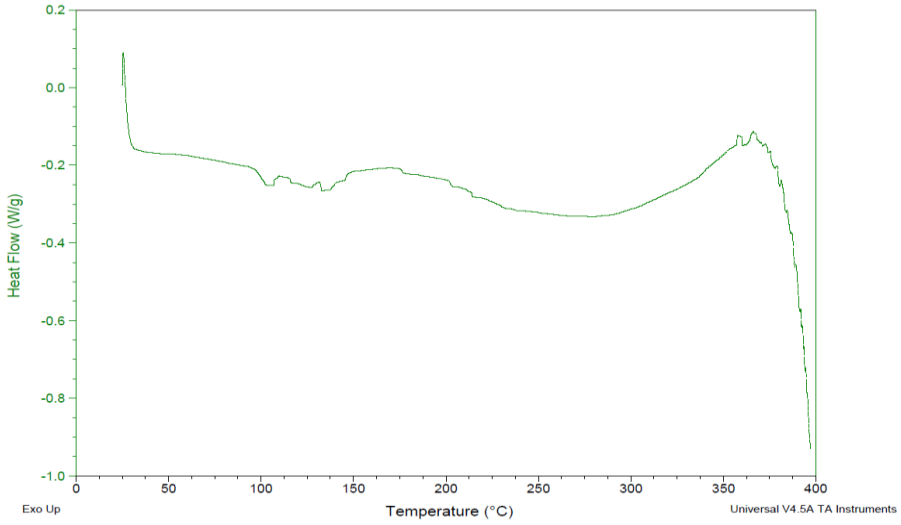

Figure 10: Typical curve of heat flow versus temperature for Z-UltraT

Glass transition temperatures of about 125°C and 144°C were evaluated for Z-ABS and Z-UltraT, respectively.

On the other hand, TGA is a method of thermal analysis in which changes in chemical and physical properties of materials are evaluated as a function of increasing temperature at a constant heating rate, or as a function of time at a constant temperature and/or constant mass loss TGA may provide information about physical phenomena, such as second-order phase transitions, including absorption, adsorption, desorption, sublimation and vaporization.

TGA relies on a high degree of precision in three measurements: mass change, temperature, temperature change.

For this reason, the basic instrumental requirements for TGA consist of a precision balance with a pan loaded with the sample, and a programmable furnace.

The TGA apparatus continuously weighs a sample as it is heated to high temperatures.

As the temperature increases, several components of the sample can be decomposed.

Thus, the weight percentage of each resulting mass change can be measured.

Results are normally plotted with temperature on the X-axis and mass loss on the Y-axis.

Results from TGA performed on Z-ABS and Z-UltraT have been reported in terms of weight-temperature curves (Figure 11andFigure 12).

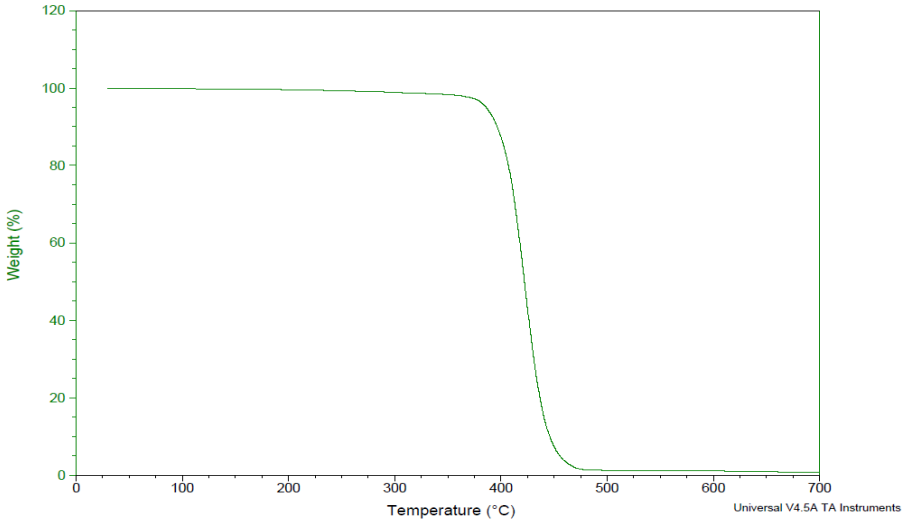

Figure 11: TGA: typical weight versus temperature curve for Z-ABS

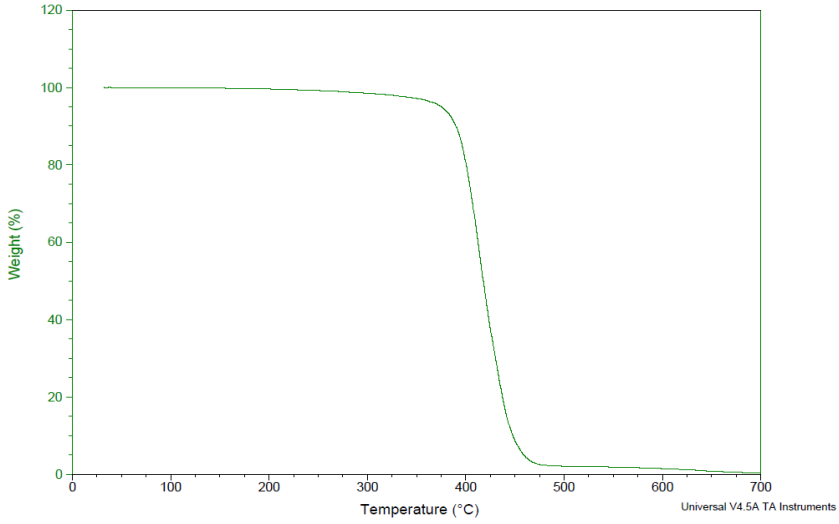

Figure 12: TGA: typical weight versus temperature curve for Z-UltraT

Results from TGA have allowed to assess the thermal stability of the materials. Accordingly, in a specific temperature range, if a species is thermally stable, no mass change is observed.

Negligible mass loss corresponds to little or no slope in the TGA trace. TGA provides the upper use temperature of a material and beyond this temperature the material begins to degrade, thus providing interesting information in terms of process parameters.

3.3. Mechanical characterization of thermoplastic materials: Flexural Tests

Three-point bending tests were performed on the different kinds of printed "building blocks" made of Z-ABS and UltraT, according to the ASTM D790 [51]. All the tests were carried out using an Instron 5566 testing machine. The support span-to-depth ratio was 16 to 1 (Figure 12 and Figure 13).

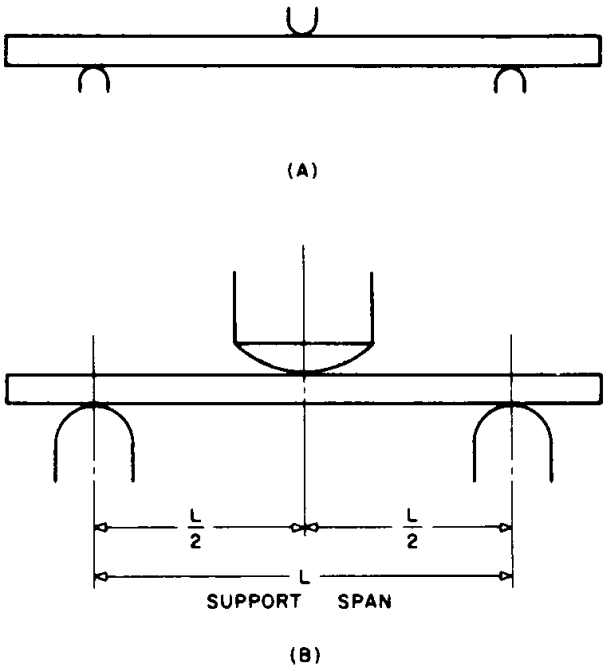

Figure 13: Figure and schematic representation of three-point bending tests

Stress (σ) and strain (ε) were evaluated as follows:

$$\sigma = \frac{3FL}{2bd^2} \tag{3.3.1}$$

$$\varepsilon = \frac{6D_f d}{L^2} \tag{3.3.2}$$

where D_f is the deflection of the specimen at the middle of the support span, F is the load at a given point of the load-deflection curve, L is the support span, b and d are the sample width and depth, respectively.

Typical stress-strain curves usually obtained from three-point bending tests was reported in Figure 14.

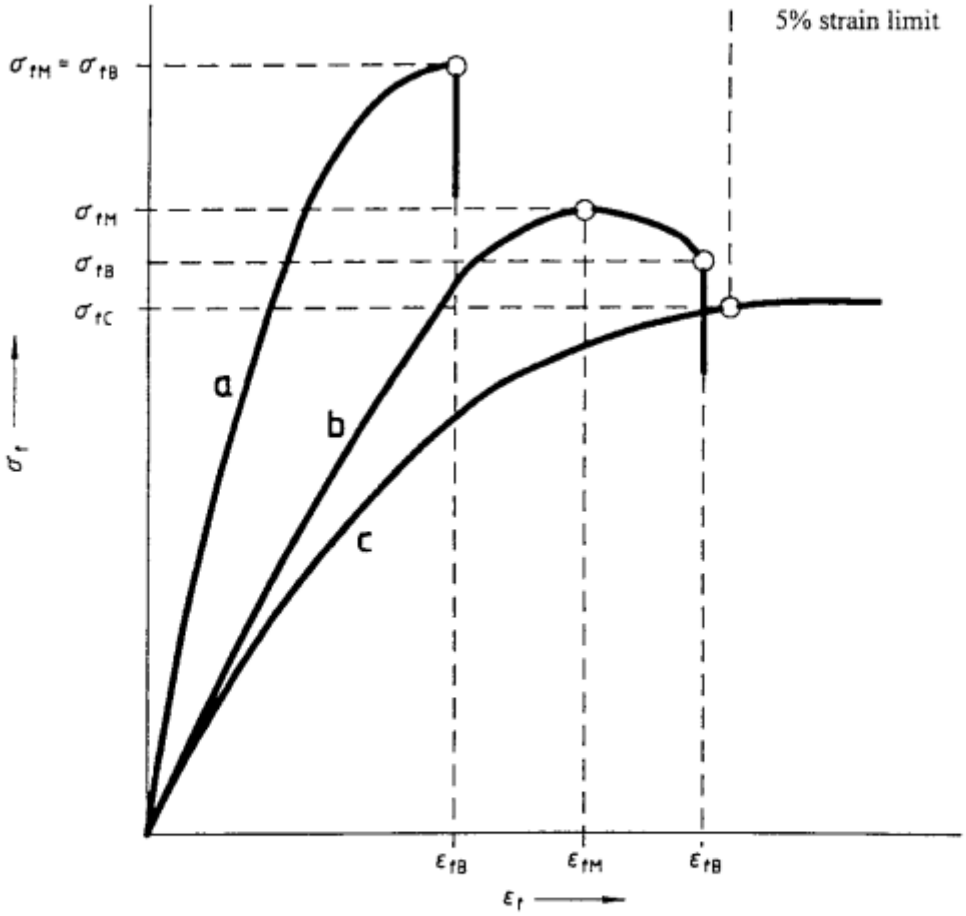

NOTE—Curve a: Specimen that breaks before yielding.
Curve b: Specimen that yields and then breaks before the 5 % strain limit.
Curve c: Specimen that neither yields nor breaks before the 5 % strain limit.

Figure 14: Typical curves of flexural stress versus flexural strain obtained from three-point bending tests, according to the ASTM D790

Three-point bending tests on the two different kinds of printed "building blocks" made of Z-ABS and Z-UltraT evidenced similar stress-strain curves (Figure 15).

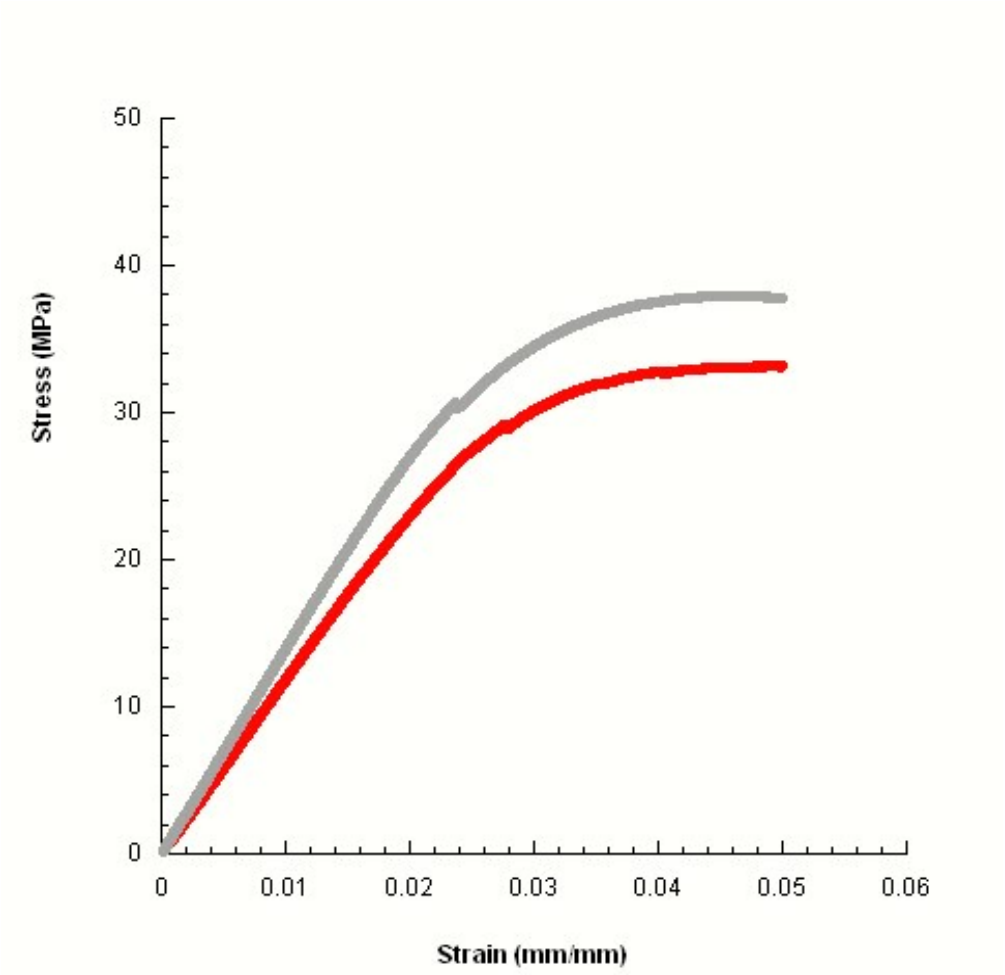

Figure 15: Typical stress-strain curves obtained from three-point bending tests on the two different kinds of printed "building blocks" made of Z-ABS (red line) and Z- UltraT (grey line)

An initial linear region of the stress–strain curve was evident. Then, a decrease of the slope was observed.

Bending modulus (i.e., the slope of the linear region of the curve) and maximum stress were evaluated and reported as mean value ± standard deviation (Table 10).

Sample	*E (MPa)*	$\sigma_{max} = \sigma_{fc}$ *(MPa)*
Z - ABS	*1202.9 ± 24.0*	*33.2 ± 0.1*
Z - ULTRA T	*1422.4 ± 19.7*	*37.9 ± 0.4*

Table 10: Results from three-point bending: modulus (E) and maximum stress (σ_{max}) reported as mean value ± standard deviation

According to the ASTM D790, as all the specimens neither yields nor break before the 5% limit, σ_{max} was equal to σ_{fc} (flexural stress at 5 % strain limit).

As reported in Table 10, Z-UltraT provided higher values of modulus and maximum stress than those obtained from Z-ABS.

3.4. DMLS powder

The aluminium alloy powder AlSI10Mg used to print the metal alloy propeller trough DMLS process was provided by EOS that provides a wide range of metal powders.

EOS Aluminium AlSi10Mg is a typical casting alloy with good casting properties and is typically used for cast parts with thin walls and complex geometry [52].

It offers good strength, hardness and dynamic properties and is therefore also used for parts subject to high loads.

Parts in EOS Aluminium AlSi10Mg are ideal for applications which require a combination of good thermal properties and low weight.

They can be machined, spark-eroded, welded, micro shot-peened, polished and coated if required.

The AlSi10Mg data sheet was reported in ANNEX III.

4. THE FABRICATION OF AM PROPELLERS

After identifying the correct printing process conditions, in relation to the material used, two propellers in Z-ABS and Z-UltraT materials was printed through FDM process and an aluminium alloy propeller has been printed in AlSi10Mg through DMLS process.

4.1. FDM propellers

The open-source RepRap Prusa Mendel Iteation 3 3D printer (Figure 16) with 0.35 mm nozzle diameter was used to fabricate the propellers in 1.75 mm Z-ABS and Z-UltraT material.

The 3D printer was assembled in two days at at Fraunhofer Joint Lab IDEAS-CREAMI (Interactive Design and Simulation - Center of Reverse Engineering and Additive Manufacturing Innovation) of the University of Naples Federico II and calibrated with an accuracy of ±10 µm using the magnetic base dial indicator, Mitutoyo 2046-08 (Mitutoyo, Japan).

The firmware open-source software Marlin and the slicing software Simplify 3D were used to generate G-code files and to command and control the 3D printer for the fabrication of the desired parts

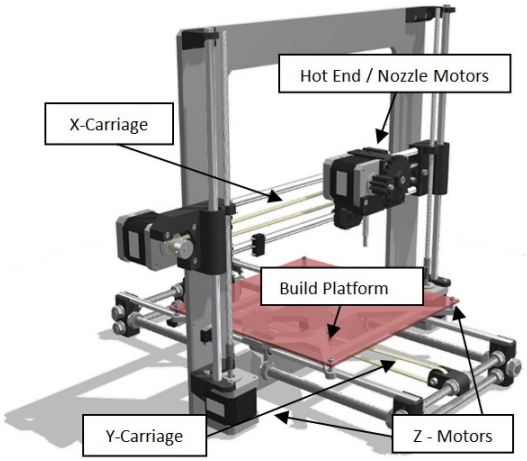

Figure 16: Rep-Rap Prusa Mendel Iteration 3

For both materials the main setup of printing process parameters were reported in Table 11.

Main Printing setting	***ABS***	***UltraT***
Layer thickness [mm]	*0.1*	*0.1*
Flow rate (%)	*105*	*105*
x-y deposition speed (mm/min)	*1800*	*1800*
z deposition speed (mm/min)	*1000*	*1000*
Fill Density (%)	*100*	*100*
Bed Temperature (°C)	*80*	*80*
Printing Temperature (°C)	*250*	*250*
Outline Overlap (%)	*15*	*15*

Table 11: Optimized setup of the main printing process parameters considered to print both the propellers

The printing process, to print both propellers in two thermoplastic materials (Figure 17) taken into account in the study has required 59 h and about 180 m of filament.

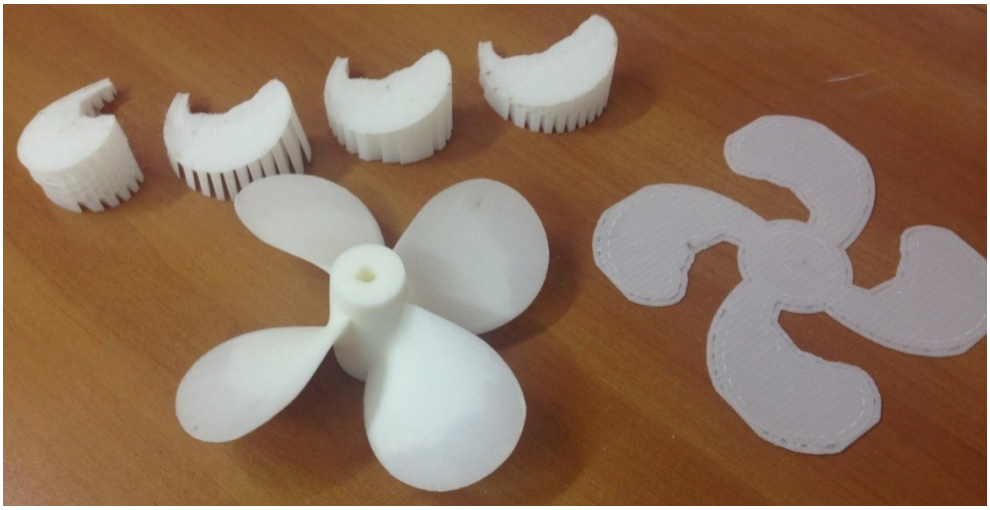

Figure 17: The propeller printed in thermoplastic materials through FDM process

4.2. DMLS propeller

The EOS M280 DMLS Printer was used to print propeller in AlSi10Mg material.
EOS has been providing also metal printing powders together with the production parameters (EOS Part Property Profiles, PPP), in order to have a producer certification, to achieve minimum certified and repeatable mechanical performances and minimize any deviation from expected values.
Although the PPP are conventionally locked, EOS provided, upon customer request, several unlocked profiles.
The latter are given with standard values which should be equivalent, according to EOS, to the corresponding ones of the locked PPPs.
Starting from these values, exposition parameters (Table 12) can be customized with respect to the actual needs, by using the Exposure Editor panel [53].

Exposure Parameter	*Value*
Laser power	*370 W*
Scanning speed	*1300 mm/s*
Layer thickness	*0.02 mm*
Hatching distance	*0.19 mm*

Table 12: Main DMLS exposure parameters

Using MAGICS software of Materialise® and RP-Tools of EOS, the STL model of the propeller was positioned and oriented on the build platform taking into account the problems due to flows of the inert gas within the print volume and the impacts due to the passage of coater (Figure 18).

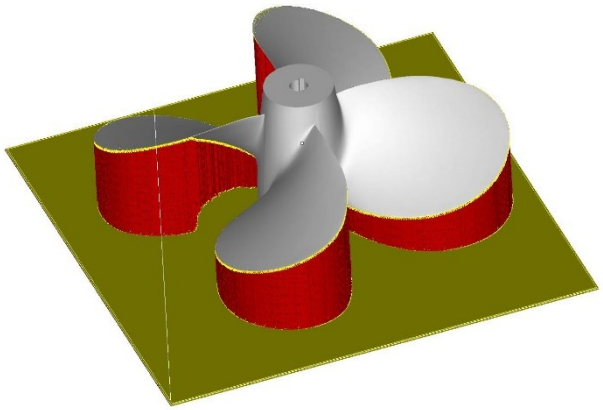

Figure 18: The preparation of DMLS printing model in Magics software

Subsequently, it was possible to create support structures, bearing in mind the countless critical issues in executing this step, such as removability, surface quality alteration and heat drain from the part.

The build platform was preheated at 200°C and the printing process has required 28 h and 30 min. In this process it was necessary a post-processing phase, with a stress relieving cycle of 2 hours at 300 °C and supports removal (Figure 19).

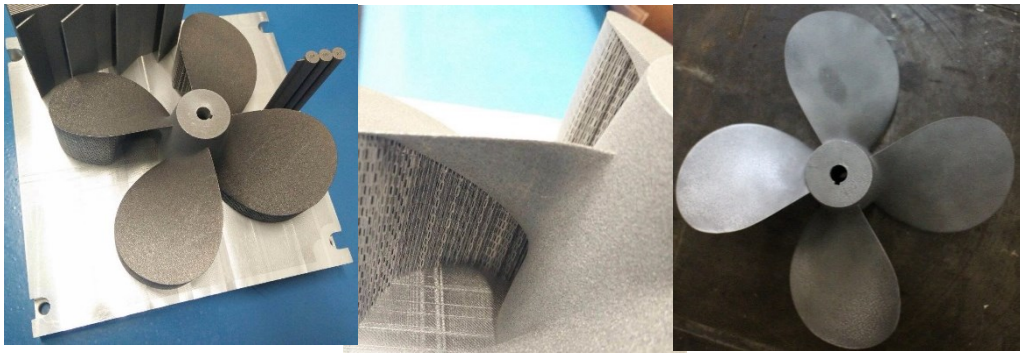

Figure 19: DMLS printed propeller before and after supports removal

5. SHAPE QUALITY INSPECTION, MORPHOLOGICAL AND ROUGHNESS EVALUATION OF THE PRINTED PROPELLERS

The subsequent stage, to manufacture of the propellers, concerning the 3D and 2D quality inspection by means of RE (Reverse Engineering) techniques and the evaluation of the morphological performance and surface roughness by AFM (Atomic Force Microscopy) analysis.

5.1. Reverse Engineering analysis

A high resolution non-contact Laser Scanner, AACMM (Articulated Arm Coordinate Measuring Machines) Faro CAM2 ScanArm HD was used to acquired and generate the cloud points of ABS (Figure 20), UltraT (Figure 21) and AlSi10Mg (Figure 22) printed propeller. The accuracy of this non-contact Reverse Engineering system is of ±25µm.
All scan data were post-processed in Geomagic Control software of 3D Systems using an iterative closest point algorithm [35], to align and minimize the distance between the clouds point and nominal CAD model.

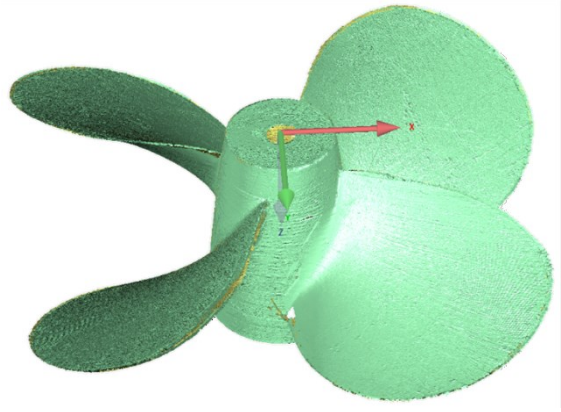

Figure 20: The cloud point of propeller printed in ABS

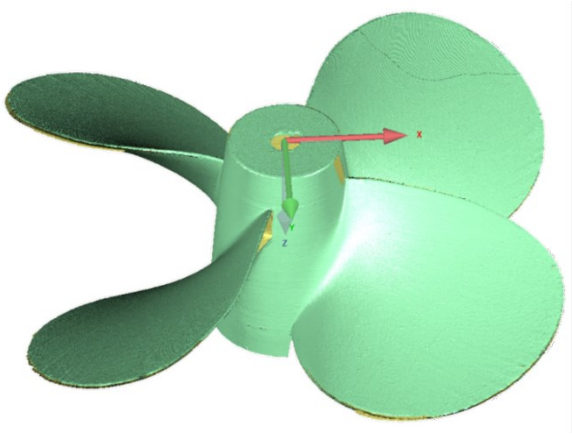

Figure 21: The cloud point of propeller printed in UltraT

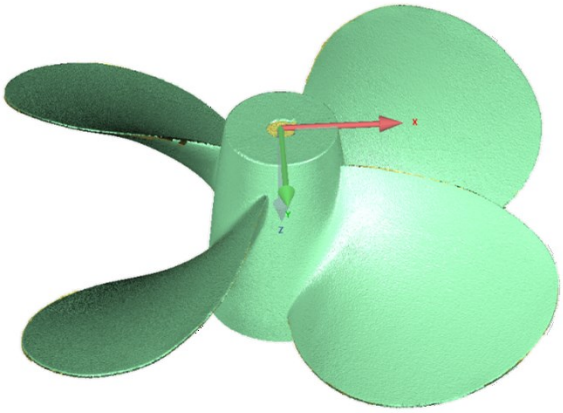

Figure 22: The cloud point of propeller printed in AlSi10Mg

As shown in Table 13 the three acquired clouds were made of a number of points between them comparable.

Cloud point	*Number of points*
AlSi10Mg	*2469684*
UltraT	*2336531*
ABS	*2392902*

Table 13: Number of points relative each acquired propeller

Based on a strictly protocol [54] and [55], to make highly repeatable the measurements, the use of well-defined features as references (see also fixtures) was considered during the alignment phase of cloud point whit nominal CAD model. Standard deviation was considered as a good measure of the accuracy.

All distances between each point clouds and the 3D CAD nominal model have been analysed. Figure 23,Figure 24Figure 25 show, the chromatic map of the distances between point clouds and nominal CAD model that were correlated to a value of Standard deviation reported in Table 14.

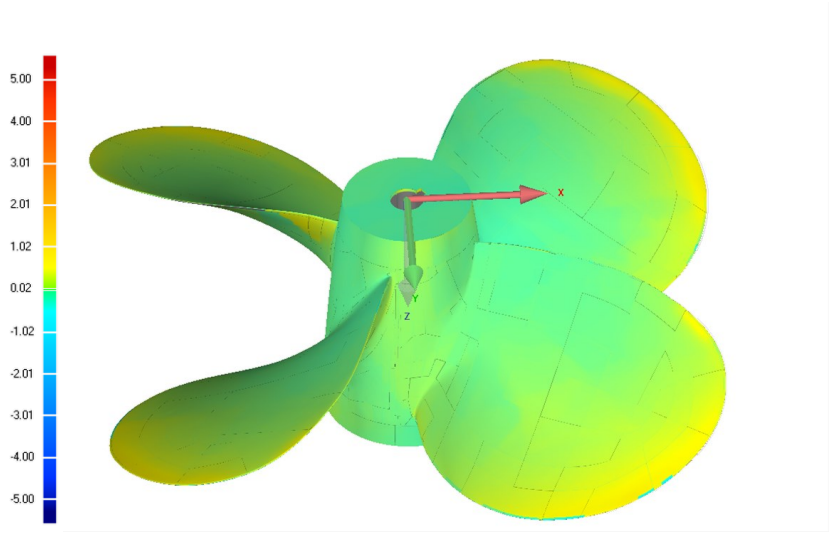

Figure 23: Graphical evaluation of distances between point cloud of propeller in AlSi10Mg and 3D CAD nominal model

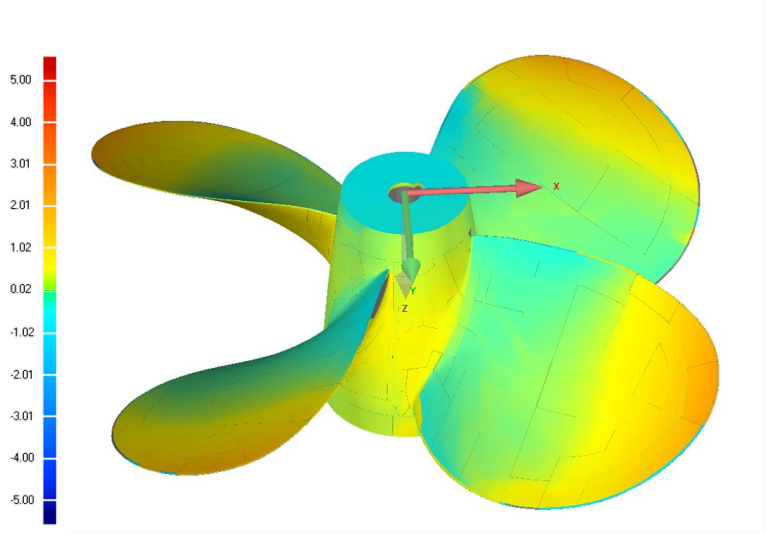

Figure 24: Graphical evaluation of distances between point cloud of propeller in UltraT and 3D CAD nominal model

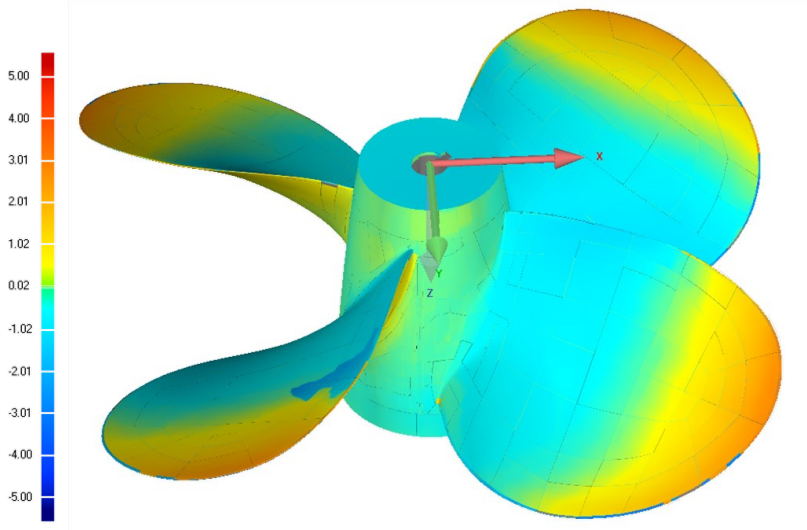

Figure 25: Graphical evaluation of distances between point cloud of propeller in ABS and 3D CAD nominal model

Cloud point	*Number of points*	
AlSi10Mg	*Average +/-*	*0.12/-0.08 mm*
	Standard Deviation	*0.14 mm*
UltraT	*Average +/-*	*0.47/-0.29 mm*
	Standard Deviation	*0.56 mm*
ABS	*Average +/-*	*0.49/-0.56 mm*
	Standard Deviation	*0.69 mm*

Table 14: Number of points relative each acquired propeller

As shown, the three-dimensional comparison between point clouds acquired by RE technique, and the CAD model, showed the greatest accuracy given by DMLS process evidenced by the lower standard deviation which has the propeller printed in AlSi10Mg, compared to propellers printed in thermoplastic materials using FDM process. In particular, between the latter two, the propeller printed in ABS presents deviations to the nominal model greater than propeller printed in UltraT.

This variation could be attributed mainly to problems due to the higher shrinkage of ABS compared to the UltraT.

The 2D deviation analysis was carried out sectioning the acquired clouds point, of each propeller, aligned with CAD model, with the plans as shown in Figure 26.

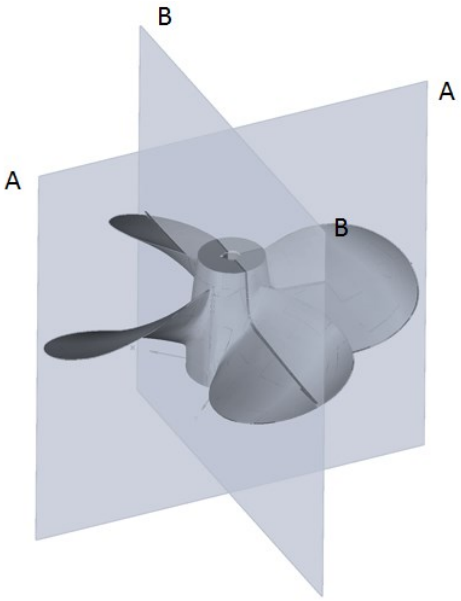

Figure 26: Planes used to sectioning the point cloud of propeller aligned with CAD model in 2D analysis

For each propeller, Figure 27, Figure 28 and Figure 29, show the comparison of 2D section, between point clouds and nominal CAD model, that were correlated to a value of Standard deviation reported in Table 14 Table 15.

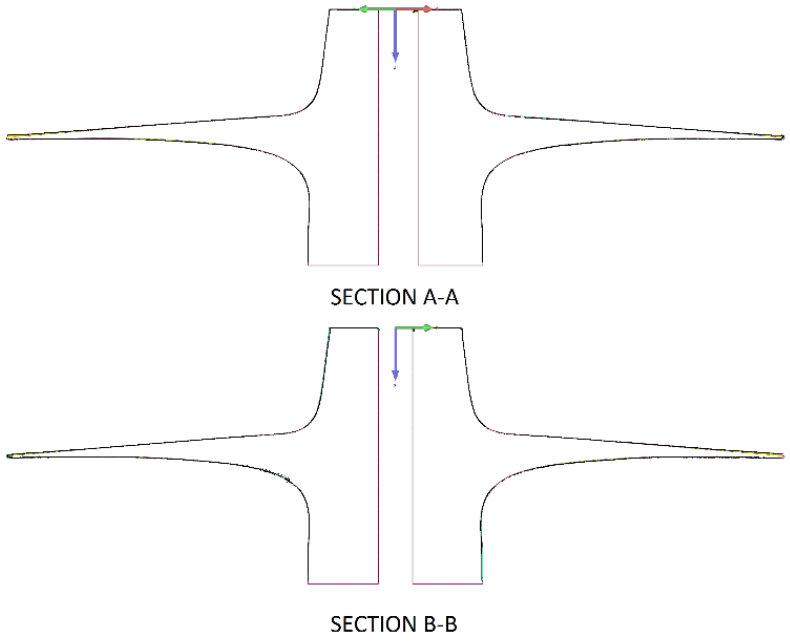

Figure 27: 2D comparison between the section of point cloud of propeller in AlSi10Mg and 3D CAD nominal model

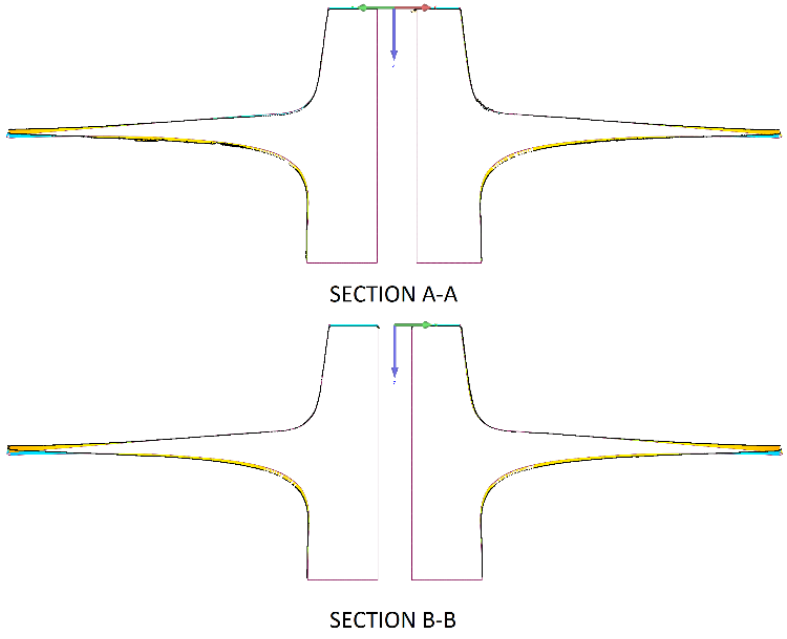

Figure 28: 2D comparison between the section of point cloud of propeller in UltraT and 3D CAD nominal model

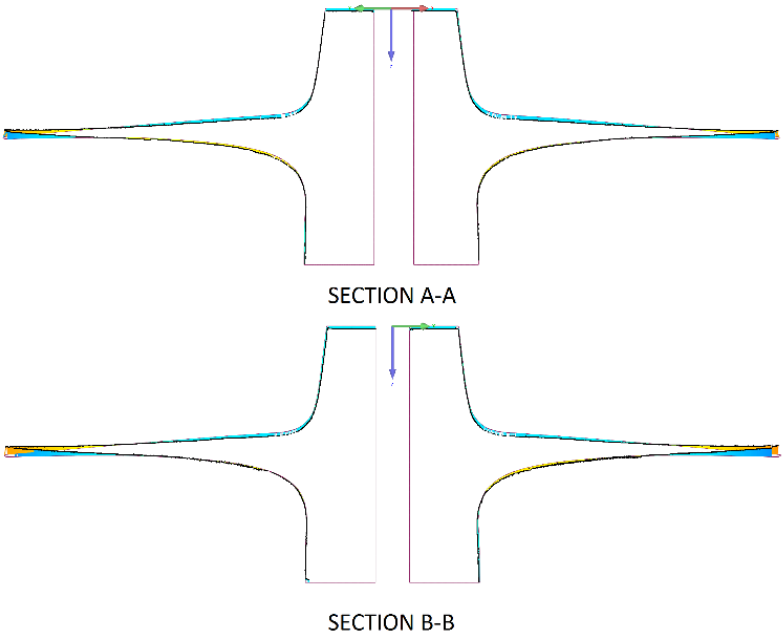

Figure 29: 2D comparison between the section of point cloud of propeller in ABS and 3D CAD nominal model

Cloud point	***Section***	***Standard Deviation***
AlSi10Mg	*A-A*	*0.15 mm*
	B-B	*0.14 mm*
UltraT	*A-A*	*0.50 mm*
	B-B	*0.57 mm*
ABS	*A-A*	*0.66 mm*
	B-B	*0.79 mm*

Table 15: 2D analysis between section of points cloud aligned to CAD model for each propeller

As shown, the comparison between the two-dimensional sections A-A and B-B, of point clouds, aligned with the CAD model, showed a substantial polar symmetry in the propeller printed in AlSi10Mg with DMLS process evidenced by the comparable standard deviations between the two section.
The propellers printed in thermoplastic materials, using the FDM process, have shown a polar asymmetry due to the shrinkage associated to this AM process and dependent on the used material.
In fact, the propeller printed in ABS showed major asymmetries, then propeller printed in UltraT.
This was evidenced by the increased difference in the standard deviation, in the comparison of the two sections, between the cloud of points and the nominal CAD model.

5.2. Atomic Force Microscopy (AFM) analysis

Atomic Force Microscopy (AFM) analysis was performed on the specimens obtained from the blade of the two polymer-based propellers.
The imaging was performed in tapping mode.
Three different AFM imaging modes can be usually considered: a) Contact mode, where the deflection of the cantilever is kept constant; b) Non-contact mode, where the tip is oscillated at the resonance frequency and the amplitude of the oscillation is kept constant; c) Tapping mode, which is somewhere between the contact and non-contact mode.
Specifically, the amplitude is set as ~ 100% of "Free" amplitude; and as ~ 50 -60% of "Free" amplitude for non-contact mode and tapping mode, respectively.
However, tapping mode provides higher resolution with minimum sample damage.
Anyway, most of times, non-contact mode is operated as tapping mode (Figure 30).

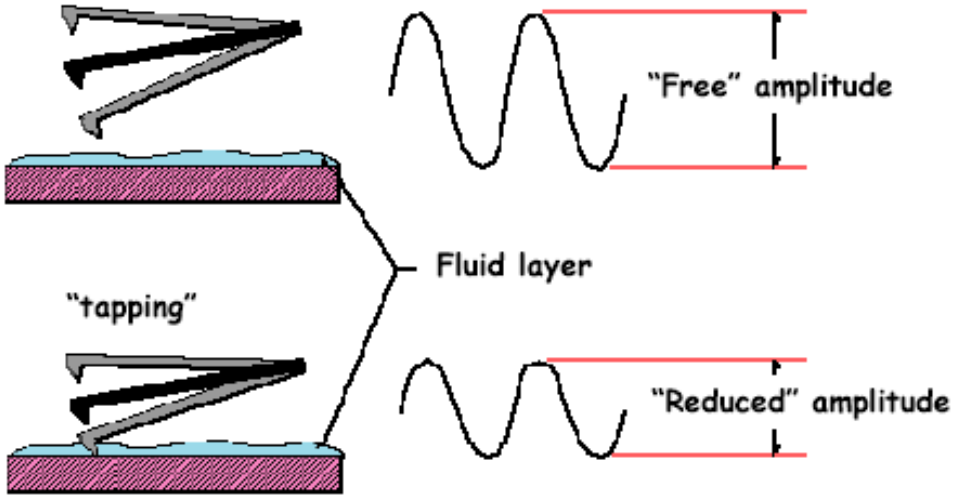

Figure 30: Schematic representation of "Free" and "Reduced" amplitude

AFM analysis has allowed to assess the morphological features, surface roughness and topography of the two samples related to the employed manufacturing technology (Figure 31 and Figure 32).

In particular, a root mean square roughness (Rms) of 0.2-1.4 nm has been evaluated.

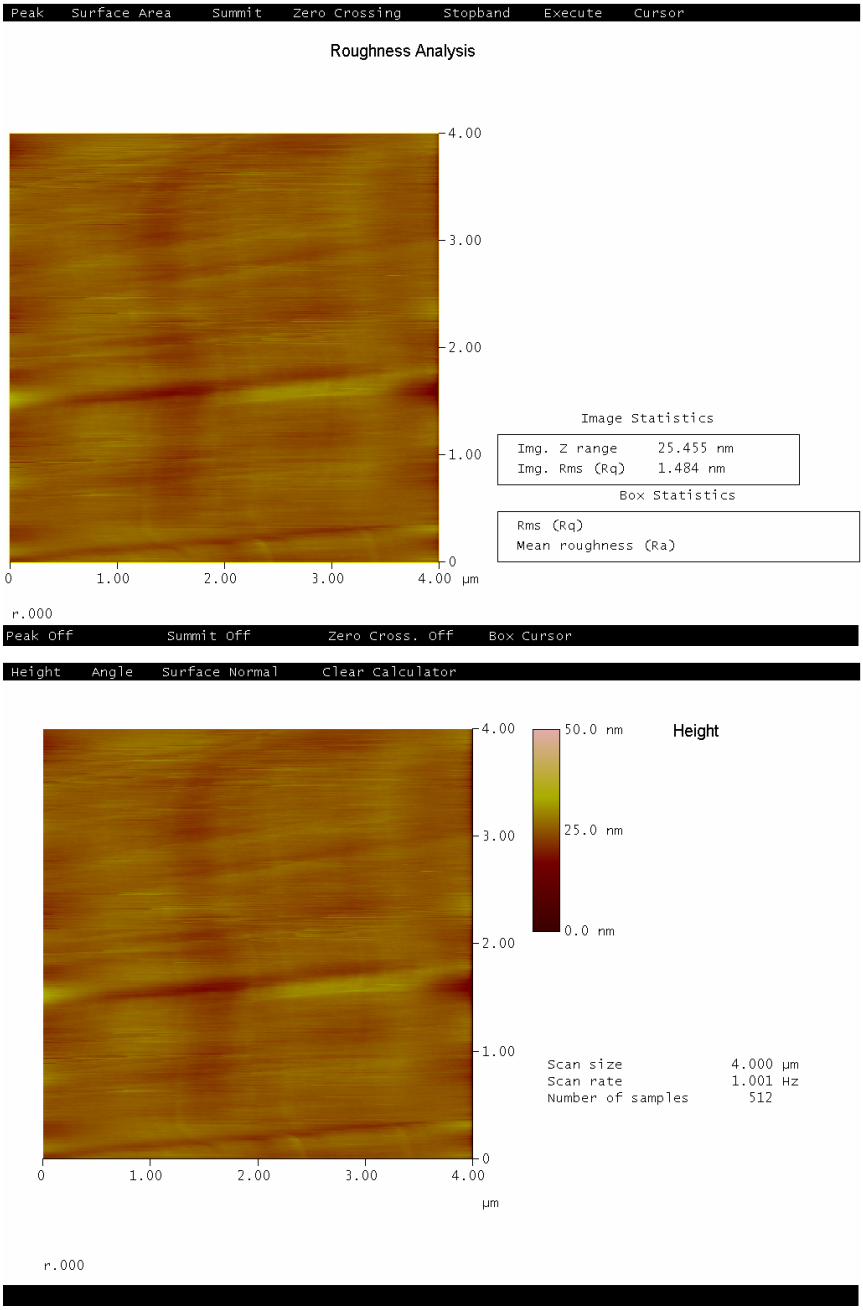

Figure 31: Results obtained from AFM performed on Z-ABS: roughness analysis

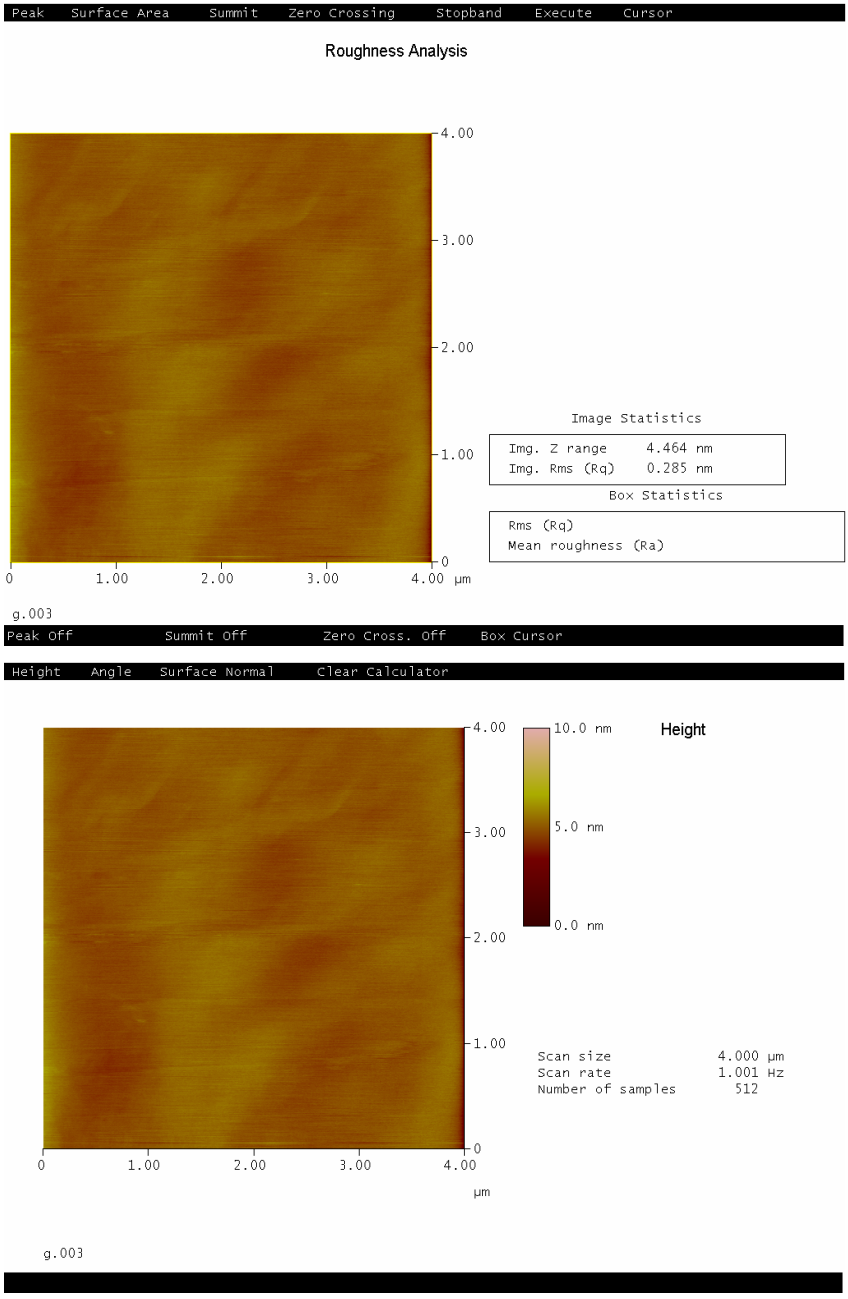

Figure 32: Results obtained from AFM performed on Z-UltraT: roughness analysis

6. MECHANICAL CHARACTERIZATION OF PRINTED PROPELLERS

To evaluate the mechanical characteristics of the printed propellers, numerical and experimental tests have been carried out.

The evaluation of the loads and their application point, to apply in experimental flexural test, have been performed numerically using a CFD code in order to have reliable data as possible.

The numerical model was validated by simulating the propeller in open water condition at nine values of the advance coefficient J and correlating and comparing the results to corresponding experimental values, in terms of the dimensionless thrust K_T and torque K_Q coefficients, to the INSEAN experimental result

6.1. Evaluation of mechanical load condition through numerical analysis (CFD)

The hydrodynamic characteristics and the loads acting on the propeller blades have been identified using a general-purpose commercial CFD software Star CCM+ of CD-adapco based on the Reynolds Averaged Navier-Stokes (RANS) equation.

The shear-stress transport (SST) k-ω model developed by Menter is chosen as the turbulence model [56].

The fluid is assumed to be viscid and incompressible with turbulent viscous regime.

All-y+ wall treatment, a hybrid method of high-y^+ wall treatment approach, in which the near-wall cell centroid should be placed in the log-law region ($30 \leq y^+ \leq 100$) and low-y^+ wall treatment, that require a sufficient mesh to resolve the viscous sublayer ($y^+ \approx 1$) was used to give accurate results.

Indicating with D (m) the propeller diameter, the boundary box dimension and boundary condition were shown in Figure 33 andFigure 34.

Considering the feasibility and computational efficiency, the domain was divided into two parts, which were meshed by unstructured grids strategy.

The rotation of the propeller, set to 11.78 rps (according to experimental data) was modelled using Moving Reference Frames (MRF) that are a reference frames that can rotate and translate with respect to the laboratory reference frame [57] [58].

Due to the complicated shape of the propeller blades, the flow field near the propeller was meshed with a refinement.

For the velocity at the blade tip is faster than that at the hub, the region around the blade tip was meshed with smaller elements of size at about 2% of base size.

Three boundary layers were grown from the blade surface with 1.5 of stretching ratio of the layers.

The first layer grid's cell height from the solid surface was approximate of 1% of base size.

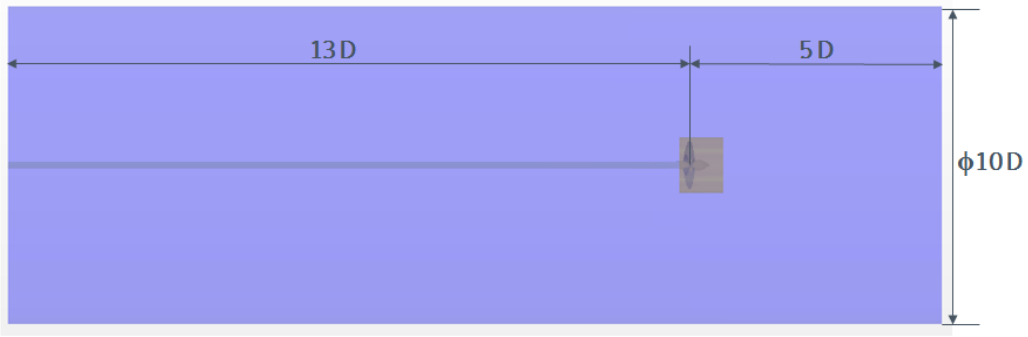

Figure 33: Numerical domain dimensions

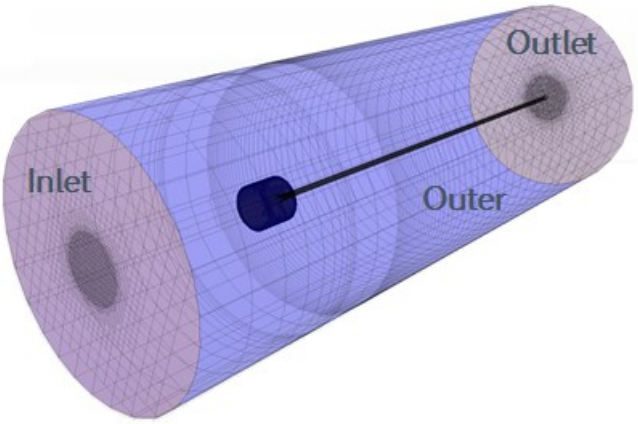

Figure 34: Boundary condition of numerical domain

The surface grids on the propeller blade and the boundary layer grids was shown in Figure 35 andFigure 36.

The size of the rotating grid, near to the propeller, has 1716496 of unstructured cells while the number of cells of static grid of outer field was 665803.

For each J, the simulation was performed for a time of 4 s with a time step set to 0.001 s, coinciding to a 4° of angle increment of propeller blades.

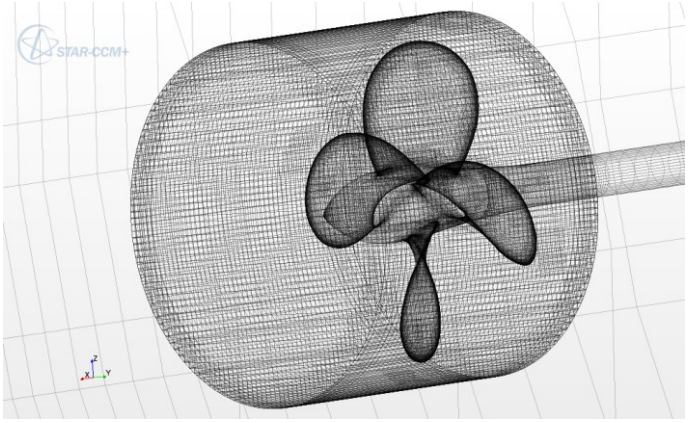

Figure 35: Rotating region of numerical domain

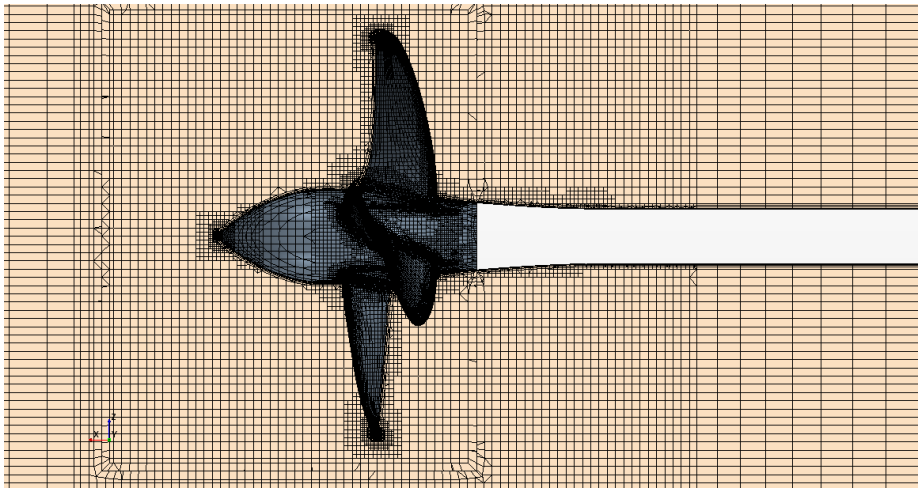

Figure 36: Boundary layer grids around propeller domain

The numerical result of CFD simulation was reported in Table 16 while the comparison between numerical and experimental data were reported in Table 17 andTable *18* and plotted in

Figure 37 Figure 38.

J	***V [m/s]***	***KT $_{CFD}$***	***10*KQ $_{CFD}$***	***Q (N·m)***	***T (N)***
0.000	*0.000*	*0.533*	*0.865*	*7.286*	*197.522*
0.326	*0.875*	*0.411*	*0.679*	*5.716*	*152.333*
0.560	*1.500*	*0.297*	*0.518*	*4.360*	*110.097*
0.653	*1.750*	*0.250*	*0.453*	*3.814*	*92.794*
0.746	*2.000*	*0.203*	*0.386*	*3.256*	*75.351*
0.886	*2.375*	*0.133*	*0.284*	*2.388*	*49.260*
0.979	*2.625*	*0.087*	*0.213*	*1.795*	*32.362*
1.026	*2.750*	*0.065*	*0.177*	*1.488*	*24.006*
1.166	*3.125*	*-0.007*	*0.054*	*0.453*	*-2.627*

Table 16: Results of CFD simulation

This results have been correlated to experimental J trough interpolation with a fifth degree polynomials defined as:

$$K_T(J) = a_0 + a_1 J + a_2 J^2 + \dots a_5 J^5 \qquad (6.1.1)$$

were

a_0=0.533; a_1=-0.2693; a_2=-0.3737; a_3=0.1183; a_4=0.1765; a_5=-0.1076

and

$$K_Q(J) = b_0 + b_1 J + b_2 J^2 + \dots b_5 J^5 \quad (6.1.2)$$

were

b_0=0.8649; b_1=-0.438; b_2=-0.5496; b_3=0.4702; b_4=-0.0840; b_5=-0.0665

The relative percentage errors of the computed K_T (Table 17) and K_Q (Table 18) coefficients were defined as:

$$\Delta K_T(\%) = 100 \cdot \frac{K_{T,CFD} - K_{T,EXP}}{K_{T,EXP}} \quad (6.1.3)$$

and

$$\Delta K_Q(\%) = 100 \cdot \frac{K_{Q,CFD} - K_{Q,EXP}}{K_{Q,EXP}} \quad (6.1.4)$$

where $K_{T,\,CFD}$, $K_{Q,\,CFD}$ were the numerical values and $K_{T,\,EXP}$, $K_{Q,\,EXP}$, the experimental values.

J	***$K_{T\ EXP.}$***	***$K_{T\ CFD}$***	***ΔK_T (%)***
0.000	*0.533*	*0.533*	*0.00*
0.348	*0.408*	*0.401*	*1.70*
0.546	*0.317*	*0.304*	*4.01*
0.646	*0.269*	*0.254*	*5.72*
0.747	*0.222*	*0.203*	*8.76*
0.895	*0.150*	*0.129*	*14.06*
0.970	*0.111*	*0.092*	*17.13*
1.020	*0.084*	*0.067*	*19.87*
1.145	*0.017*	*0.004*	*76.99*

Table 17: Comparison between experimental and numerical K_T

J	$K_{Q\ EXP.}$	$K_{Q\ CFD}$	ΔK_Q (%)
0.000	0.871	0.865	0.70
0.348	0.674	0.664	1.46
0.546	0.541	0.528	2.45
0.646	0.472	0.457	3.13
0.747	0.405	0.385	4.84
0.895	0.294	0.278	5.56
0.970	0.234	0.221	5.73
1.020	0.194	0.181	6.72
1.145	0.088	0.073	16.56

Table 18: Comparison between experimental and numerical K_Q

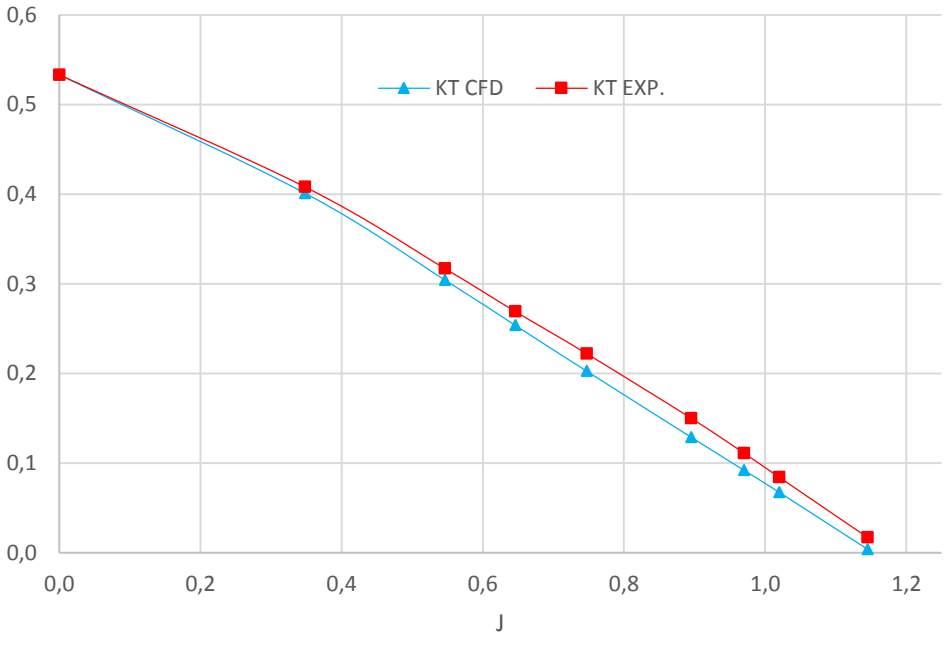

Figure 37: Comparison between numerical and experimental value of K_T

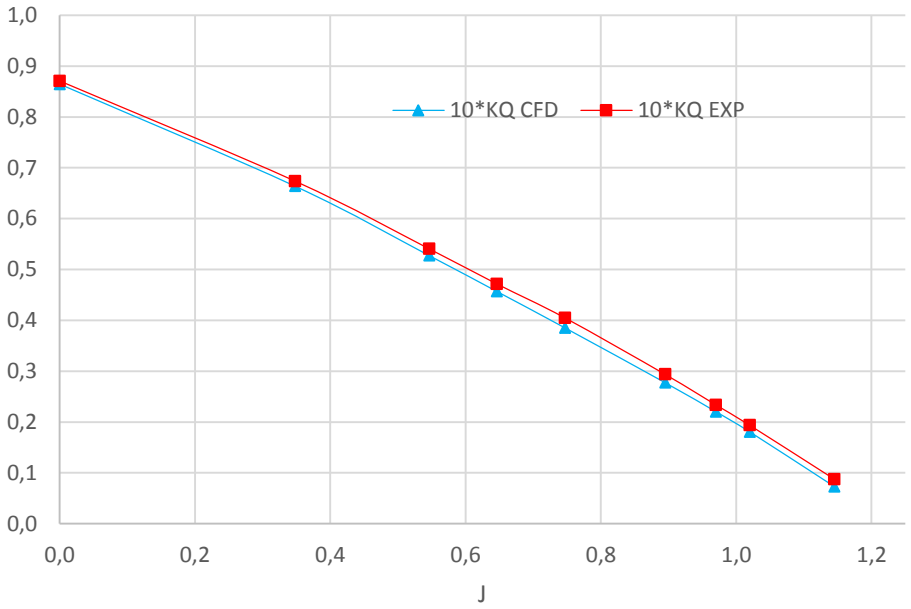

Figure 38: Comparison between numerical and experimental value of K_Q

Considering the most critical load condition of propeller work, i.e., the working condition at fixed point (J = 0), the assessments of test condition to perform in the flexural analysis, were evaluated schematizing the system of forces acting on the propeller and their application point as shown in Figure 39.

In this condition the system of forces acting on the single blade has been divided and only the axial force was considered, neglecting the other components.

For each blade, the coordinates of the center of pressure were assessed.

In that point the component of the axial force was applied in the flexural test.

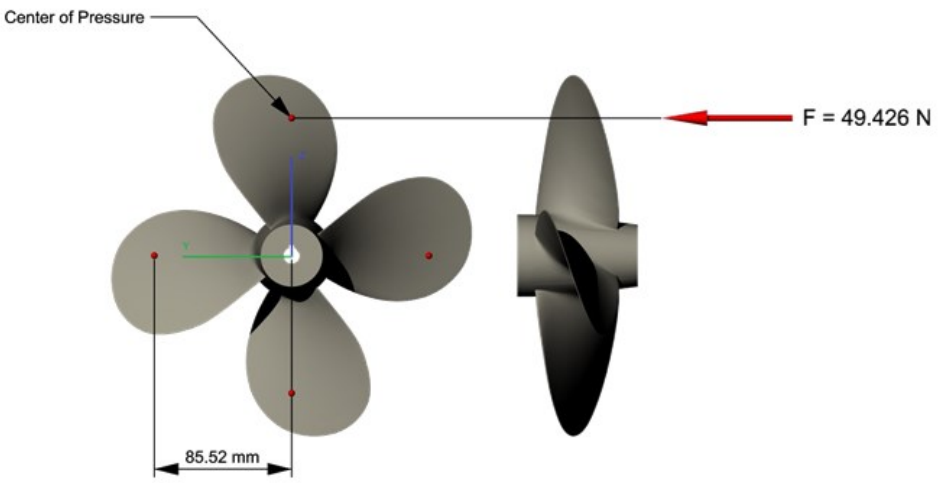

Figure 39: The application point and the force to perform in flexural test

6.2. Blade bendingl tests

Blade bending tests were experimentally performed by locally applying a load (49.426 N), considering the coordinates of the center of pressure obtained from modelling.
The tests were carried out using an Instron 5566 testing machine (Figure 40).

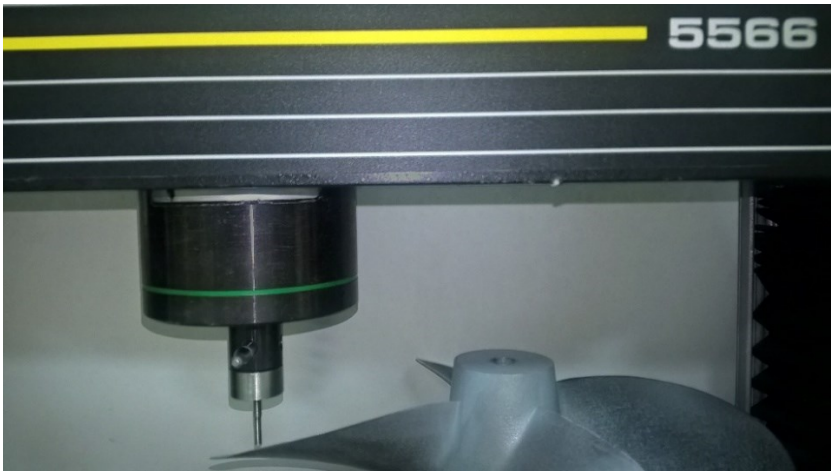

Figure 40: An image of the experimental test performed on the blade

The obtained displacement values were reported in the following Table 19.

Material	***Load [N]***	***Displacement [mm]***
Z-ABS	*49,426*	*1,90±0,14*
Z-UltraT	*49,426*	*1,70±0,14*
AlSi10Mg	*49,426*	*0,56±0,06*

Table 19: Results obtained from the experimental tests: displacement reported as mean value ± standard deviation

Table 19 clearly evidences a higher flexibility and compliance of the polymer-based devices if compared to the metal one.

7. HYDRODYNAMIC PERFORMANCE ANALYSIS OF THE PRINTED PROPELLERS

Following the current procedures recommended by the International Towing Tank Conference (ITTC), the towing tank open water propeller tests were performed with the sampling frequency of 1 kHz, on the three printed propellers.
The comparison of hydrodynamic performance between them and benchmark, in terms of trust and torque, were carried out.

7.1. Towing Tank Tests

The experimental tests have been performed in the towing tank in Naval Section of Department of Industrial Engineering of the University of Naples "Federico II".
The towing tank is 136.5 m long, 9 m large and 4.5 m deep.
It allows a maximum speed of 10 m/s with an acceleration of 1 m/s^2 and a deceleration of 3 m/s^2.
The towing tests have been performed by using a propeller dynamometers called H29.
ANNEX IV contains the device fact sheets.
As suggested by the ITTC procedures [7], the Reynolds number (Re) of the open water propeller tests was calculated relatively to cord measured at 0.7 of the radius ($Re_{0.7R}$), as it, generally, considered representative of the performance of the entire blade.
The procedure used to obtain the dimensionless thrust K_T and torque K_Q coefficients, as a function of the advance coefficient J, previously defined, involves to vary the tank dynamometer speed V and keeping constant the propeller revolutions n.
This methodology ensures that the $Re_{0.7R}$ not vary much from zero to maximum J of test because the rotational speed vector, of the cord at 0.7 of the radius, is proportionally greater than of the advancement speed V so, their sum, is not very influenced by the second addendum.
The Towing Tank results, for the three printed propellers, were reported in ANNEX V

7.2. Hydrodynamic performance analysis and comparison between printed propellers and benchmark

The results of towing tank experimental test, of dimensionless K_T and K_Q coefficients, of propeller printed in AlSi10Mg trough DMLS process, reported in Table 27 of ANNEX V, have been interpolated with a fifth degree polynomials defined as:

$$K_T(J) = a_0 + a_1 J + a_2 J^2 + \dots a_5 J^5 \quad (7.2.1)$$

were

a_0=0.5139; a_1=-0.2397; a_2=-0.5297; a_3=0.4855; a_4=-0.1334; a_5=-0.0223

and

$$K_Q(J) = b_0 + b_1 J + b_2 J^2 + \dots b_5 J^5 \quad (7.2.2)$$

were

b_0=0.8677; b_1=-0.4253; b_2=-0.5555; b_3=0.6392; b_4=-0.2911; b_5=0.0083

and correlated to the advance coefficients J of experimental performance characteristics of the INSEAN benchmark propeller Table 28.

For the propellers printed in thermoplastic materials trough FDM process, the results of dimensionless K_T and K_Q coefficients, have been interpolated with a fifth degree polynomials defined for UltraT as:

$$K_T(J) = a_0 + a_1 J + a_2 J^2 + \dots a_5 J^5 \quad (7.2.3)$$

were

a_0=0.5687; a_1=-0.2362; a_2=-0.8114; a_3=1.0394; a_4=-0.6023; a_5=0.1226

and

$$K_Q(J) = b_0 + b_1 J + b_2 J^2 + \dots b_5 J^5 \quad (7.2.4)$$

were

b_0=1.227; b_1=-0.4461; b_2=-1.269; b_3=1.9875; b_4=-1.3542; b_5=0.3198

while for ABS defined as:

$$K_T(J) = a_0 + a_1 J + a_2 J^2 + \dots a_5 J^5 \quad (7.2.5)$$

were

a_0=0.5687; a_1=-0.2362; a_2=-0.8114; a_3=1.0394; a_4=-0.6023; a_5=0.1226

and

$$K_Q(J) = b_0 + b_1 J + b_2 J^2 + \dots b_5 J^5 \quad (7.2.6)$$

were

b_0=1.227; b_1=-0.4461; b_2=-1.269; b_3=1.9875; b_4=-1.3542; b_5=0.3198.

The correlation to the advance coefficients J of experimental performance characteristics of the INSEAN benchmark propeller were reported in Table 28 of ANNEX V for UltraT propeller and in Table 32 of ANNEX V for ABS propeller.

In Figure 41, were plotted and compared the results of hydrodynamic characteristics, in terms of thrust generated by the propellers trough the dimensionless coefficient K_T while, in Figure 42, were plotted and compared the results of hydrodynamic characteristics, in terms of torque absorbed by the propellers trough the dimensionless coefficient K_Q.

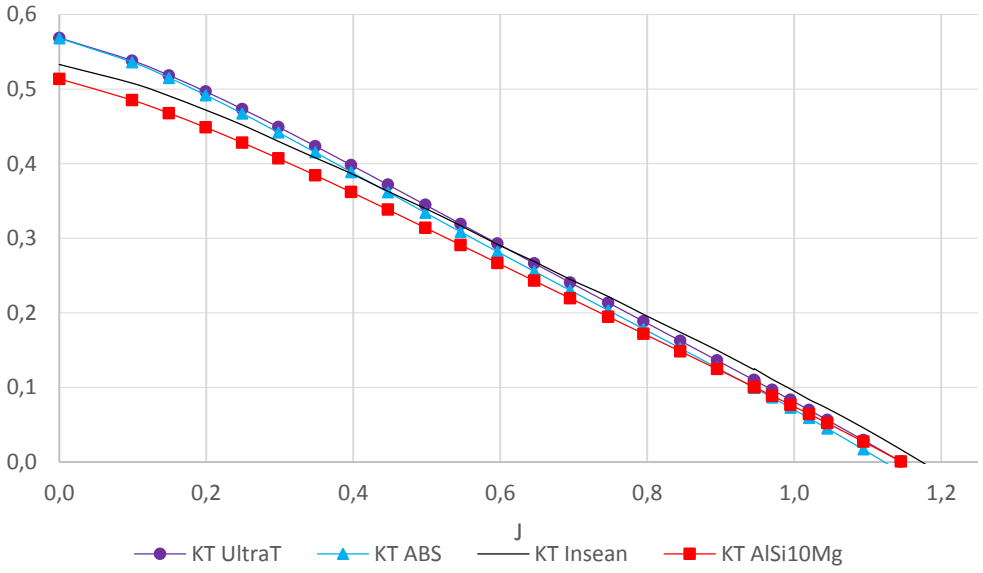

Figure 41: Comparison of K_T coefficient of the three printed propeller to the benchmark

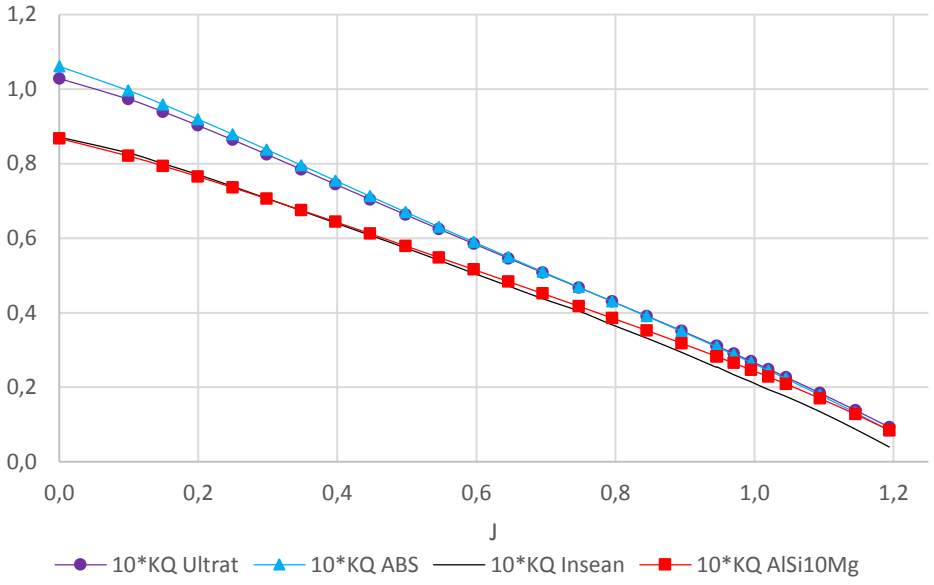

Figure 42: Comparison of K_Q coefficient of the three printed propeller to the benchmark

The comparison between the dimensionless thrust coefficients, K_T, shows a substantial coincidence of the characteristic curves.

The curves of K_T, relative to the propellers printed in UltraT and ABS, coincided between them and respect to the benchmark, with slightly higher values at low values of J.

The curve of K_T relative to the propeller printed in AlSi10Mg presents, for each J, lower values compared to the benchmark of an amount almost constant.

Instead, as regards the characteristics curves relating to torque absorption, for propellers in ABS and UltraT, the curves of the K_Q coincided between them and, compared to the benchmark, have higher values relatively to low J, or, when propeller working in load conditions.

For the propeller printed in AlSi10Mg, the characteristic curve of the K_Q generally coincided to the benchmark with slightly higher values to high J, or, when the propeller works discharge.

The differences in performance between the printed propellers and the benchmark can be attributed to:

- variations in geometry, compared to the original propeller, due to the RE process that led to the geometry to be used for the generation of the initial CAD model;
- geometrical variations, quantified in the shape control phase by RE techniques, due to the printing process;
- the polar asymmetries due to retreats relatively to materials and printing processes considered;
- the mechanical characteristics detected by flexural test;
- the morphological characteristics and the surface roughness measured by AFM analysis.

Concerning to propeller manufactured in thermoplastic materials, the main differences to the benchmark, were found in the increases of absorbed torque at low values of J, or, when the propellers working under load.

In this condition, as a result also from the flexural tests, the variations can be mainly attributed to the deformation of the material used which involves a change in effective pitch of the blade section [59].

In the flexural test, this problem is not found in the propeller made of aluminum alloy.

For the latter, however, it was found a high value relative to the surface roughness compared to the benchmark propeller.

This problem could be the principal cause of the constant less value in K_T of AlSi10Mg from the benchmark.

Also, having carried out the measures to 1 kHz sampling frequency, the Fast Fourier Transforms (FFT) method was used to analyze the spectral characteristics of torque of the printed propellers for three values of the advance coefficient J (Figure 43Figure 44Figure 45).

Spectral amplitude was obtained applying an averaging technique with a hamming window. The field of amplitude of interest has required the application of a band filter to below 10 Hz and above 50 Hz.

Also, having carried out the measures to 1 kHz sampling frequency, the Fast Fourier Transforms (FFT) method was used to analyze the spectral characteristics of torque of the printed propellers for three values of the advance coefficient J.

Spectral amplitudes were obtained applying a averaging technique with a Hamming window. The field of amplitude of interest has required the application of a band filter to below 10 Hz and above 50 Hz.

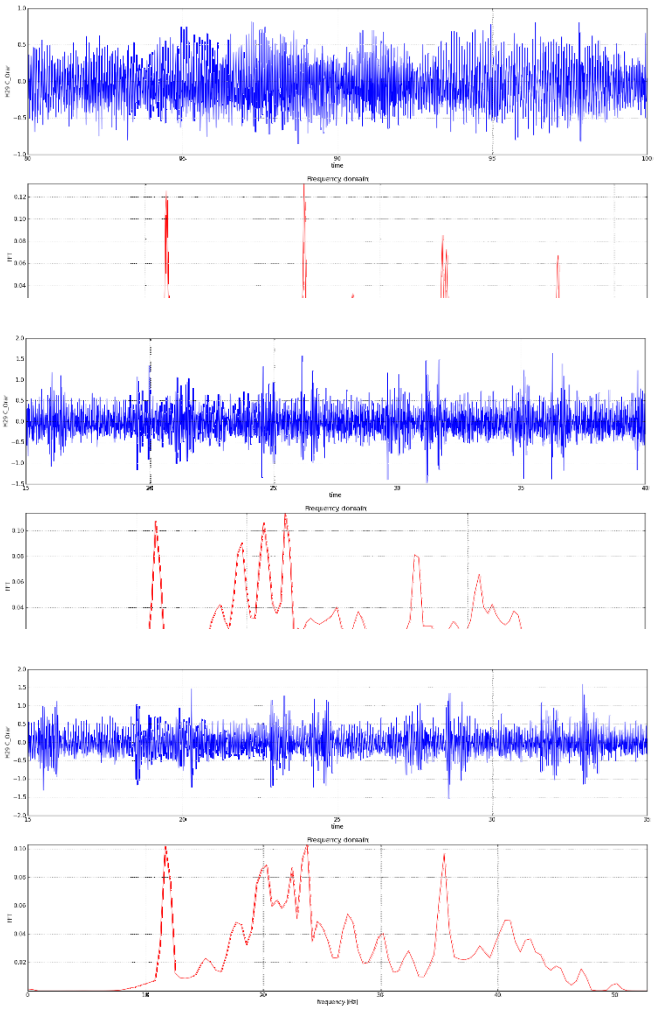

Figure 43: Time-frequency analysis of experimental data of AlSi10Mg propeller

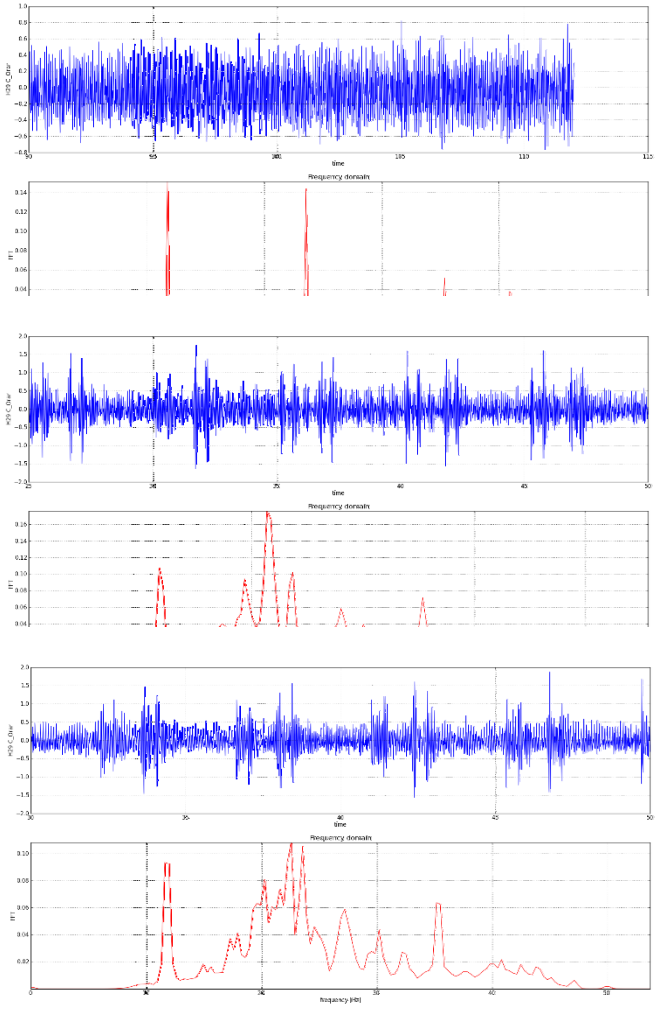

Figure 44: Time-frequency analysis of experimental data of UltraT propeller

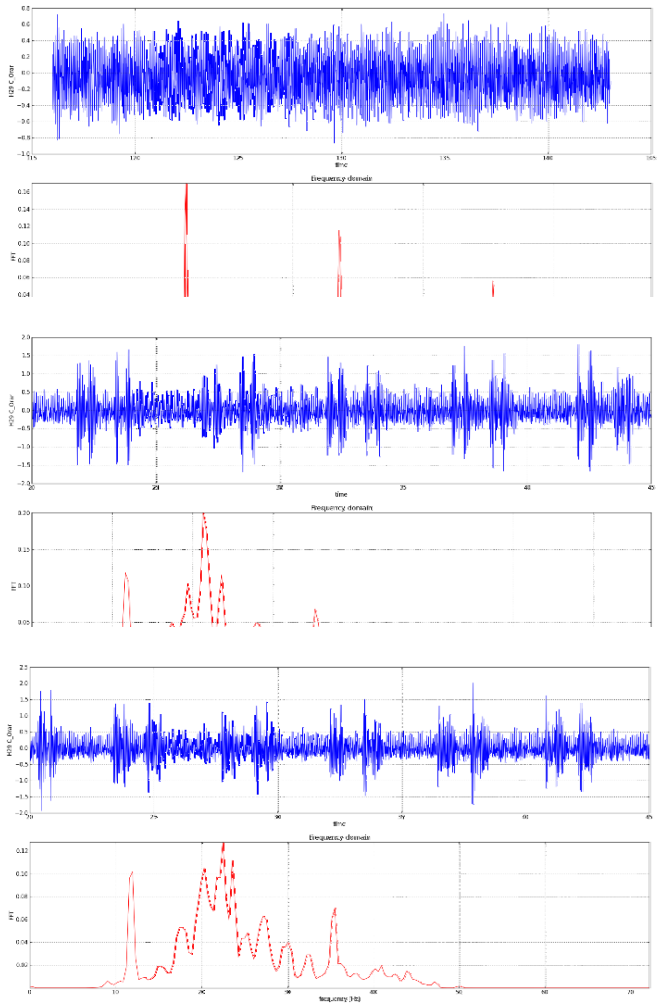

Figure 45: Time-frequency analysis of experimental data of ABS propeller

As shown in Figure 43,Figure 44Figure 45 when the propeller is loaded, at low J, there are four increments of amplitude coincident with the modal relative to the blade passages in all the printed propellers.

For the values of J, for which the propellers were more discharges, there was a increment of amplitude, for the propellers in thermoplastic material, coinciding with the second modal, or, with two times the blade passing.

This phenomena, which could be attributed to residual polar asymmetries due to shrinkage associated with AM processes, has been the input to perform the two-dimensional analysis on the propeller sections that confirmed this assumption.

Furthermore, this effect was not noticeable at low values of J due to other effects such as the bending of the blades that were predominant.

CONCLUSIONS

The main objective of this research work has regarded the analysis and the comparison of hydrodynamic performance of marine propellers manufactured using two Additive Manufacturing techniques.
In particular, a Direct Metal Laser Sintering, (DMLS), was used to print an aluminium alloy propeller and a Fused Deposition Modeling, (FDM), was used to print two propellers in different types of thermoplastic materials.

The results obtained can be reassumed in the following considerations:

- The study of printing parameters and the accurate physical-chemical and mechanical tests on the thermoplastic materials take into account, have allowed to optimize the process conditions
- Mechanical analysis and AFM test made it possible to evaluate mechanical and morphological performance.
- The evaluation of the printed propellers was carried out by combining their morphological and mechanical data with the comparison of their performance in respect to the benchmark.
- Also, having carried out the measures to 1 kHz sampling frequency, were evaluated the effects, on the hydrodynamic performance of the propellers, of the residual polar asymmetries due to shrinkage associated to AM process.

The final analysis showed that the substantial adequacy of the AM propellers realized, for most of the studies carried out in Towing Tank.
This is due both to the reduced deviations from the nominal model, that to verified constancy of performance offered by each prototype.

Future work on this research will improve the study of effect of roughness on the hydrodynamic performance of printed propeller and evaluate the performance of propeller printed trough FDM process, using a polymeric composite reinforced with nanoparticles, in order to increase the mechanical characteristics and to make their hydrodynamic performance how much closer to metal propellers manufactured with classic processes.

SYMBOLS

b	sample width
D	propeller diameter
d	sample depth
D_f	deflection
d_i	distance between the correlated points
ε	strain
F	load
J	advance coefficient
KQ	dimensionless torque coefficients
KT	dimensionless thrust coefficients
L	support span
n	propeller rotational speed
N	number of points
Q	torque
Re	Reynolds number
T	thrust
V	speed
ρ	water density
σ_{fc}	flexural stress at 5 % strain limit
σ_{max}	maximum stress

ACRONYMS

(3DP)	3D Printing
(AACMM)	Articulated Arm Coordinate Measuring Machines
(ABS)	Acrylonitrile-Butadiene-Styrene
(AFM)	Atomic Force Microscopy
(AM)	Additive Manufacturing
(ASTM)	American Society for Testing and Materials
(CAD)	Computer Aided Design
(CFD)	Computational Fluid Dynamic
(CR)	Contribution Ratio
(DMD)	Direct Metal Deposition
(DMLS)	Direct Metal Laser Sintering
(DOD)	Drop On Demand
(DOE)	Design of Experiment
(DSC)	Differential Scanning Calorimetry
(EBM)	Electron Beam Melting
(FFT)	Fast Fourier Transforms
(FDM)	Fused Deposition Modeling
(IGES)	Initial Graphics Exchange Specification
(ITTC)	International Towing Tank Conference
(LENS)	Laser Engineered Net Shaping
(LMD)	Laser Metal Deposition
(LOM)	Laminated Object Manufacturing
(MJM)	Multi Jet Modeling,
(PPP)	Part Property Profiles
(RE)	Reverse Engineering
(RMS)	Root Mean Square
(RP)	Rapid Prototyping
(TGA)	Thermogravimetric Analysis
(SHS)	Selective Heat Sintering
(SLA)	Stereolithography
(SLM)	Selective Laser Melting

(SLS) Selective Laser Sintering

(STL) Stereolithography

(UAM) Ultrasonic Additive Manufacturing

ANNEX I

J	K_T	$10*K_Q$	n [rps]
0	0.533	0.871	11.788
0.099	0.508	0.829	11.788
0.149	0.491	0.8	11.788
0.199	0.472	0.771	11.788
0.249	0.452	0.739	11.788
0.298	0.43	0.707	11.788
0.348	0.408	0.674	11.788
0.397	0.387	0.641	11.788
0.447	0.363	0.608	11.788
0.498	0.34	0.574	11.788
0.546	0.317	0.541	11.788
0.596	0.292	0.506	11.788
0.646	0.269	0.472	11.788
0.695	0.245	0.438	11.788
0.747	0.222	0.405	11.788
0.795	0.198	0.368	11.788
0.845	0.174	0.332	11.788
0.895	0.15	0.294	11.788
0.945	0.124	0.254	11.788
0.946	0.125	0.255	11.788
0.97	0.111	0.234	11.788
0.995	0.098	0.215	11.788
1.02	0.084	0.194	11.788
1.045	0.072	0.176	11.788
1.094	0.046	0.135	11.788
1.145	0.017	0.088	11.788
1.194	-0.012	0.04	11.788

Table 20: The INSEAN E779a experimental data

ANNEX II

Root Mean Square (RMS) defined by the equation (1) was considered as response:

$$RMS = \sqrt{\frac{1}{N}\sum_{i=1}^{n} d_i^{\,2}} \quad (1)$$

where d_i is the distance between the correlated points of real and nominal part and N in the number of points. This response is a good measure of the accuracy. Using the best alignment, established for the three datum, all distances between each point clouds and the 3D CAD nominal model were recorded. Figure 46 shows, for example, the chromatic map of the distances between benchmarking real and nominal part that is correlated to a value of RMS equal to 0,15 mm.

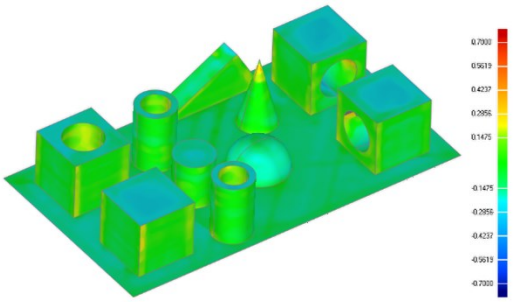

Figure 46: Graphical evaluation of distances between point cloud and 3D CAD nominal model correlated to a RMS equal to 0,15

Table 21 shows the full factorial design adopted for three factors at three levels (-1,0,1). Further, it shows the RMS values (mm) for three replicated prototypes and the sample mean and standard deviation of RMS. ANOVA table for average RMS shows that the factors A (p=0.033), B (p=0.012) and C (p=0.035) are significant with α equal to 5%, while the interactions (AB, AC, BC) are not significant (Table 22). Figure 47 shows the Contribution Ratio (CR%) of the main effects and interactions.

Prototype	Factor			Response: RMS [mm]				
				Replication			Replication	Mean
	A	B	C	1	2	3	Mean	St.Dev
1	-1	-1	-1	0.125	0.108	0.095	0.11	0.015
2	-1	-1	0	0.082	0.075	0.096	0.08	0.011
3	-1	-1	1	0.088	0.083	0.089	0.09	0.003
4	-1	0	-1	0.107	0.087	0.097	0.10	0.010
5	-1	0	0	0.086	0.089	0.082	0.09	0.004
6	-1	0	1	0.087	0.09	0.095	0.09	0.004
7	-1	1	-1	0.115	0.122	0.125	0.12	0.005
8	-1	1	0	0.107	0.105	0.105	0.11	0.001
9	-1	1	1	0.113	0.113	0.122	0.12	0.005
10	0	-1	-1	0.107	0.115	0.095	0.11	0.010
11	0	-1	0	0.086	0.091	0.098	0.09	0.006
12	0	-1	1	0.088	0.085	0.089	0.09	0.002
13	0	0	-1	0.166	0.282	0.151	0.20	0.072
14	0	0	0	0.100	0.097	0.098	0.10	0.002
15	0	0	1	0.095	0.148	0.106	0.12	0.028
16	0	1	-1	0.195	0.148	0.139	0.16	0.030
17	0	1	0	0.109	0.131	0.116	0.12	0.011
18	0	1	1	0.111	0.115	0.118	0.11	0.004
19	1	-1	-1	0.110	0.116	0.119	0.12	0.005
20	1	-1	0	0.095	0.102	0.105	0.10	0.005
21	1	-1	1	0.096	0.101	0.104	0.10	0.004
22	1	0	-1	0.109	0.114	0.114	0.11	0.003
23	1	0	0	0.108	0.141	0.138	0.13	0.018
24	1	0	1	0.116	0.112	0.122	0.12	0.005
25	1	1	-1	0.143	0.147	0.164	0.15	0.011
26	1	1	0	0.137	0.139	0.147	0.14	0.005
27	1	1	1	0.155	0.136	0.151	0.15	0.010

Table 21: Full factorial design of the three control factors replicated three times

Source	*DF*	*Seq SS*	*F*	*p-value*
A	*2*	*0.003183*	*5.35*	*0.033*
B	*2*	*0.004834*	*8.13*	*0.012*
C	*2*	*0.003126*	*5.26*	*0.035*
AB	*4*	*0.001993*	*1.68*	*0.248*
AC	*4*	*0.002518*	*2.12*	*0.17*
BC	*4*	*0.000185*	*0.16*	*0.955*
Error	*8*	*0.002379*		
Total	*26*	*0.018218*		

Table 22: Analysis of Variance for the response RMS (α=0.05)

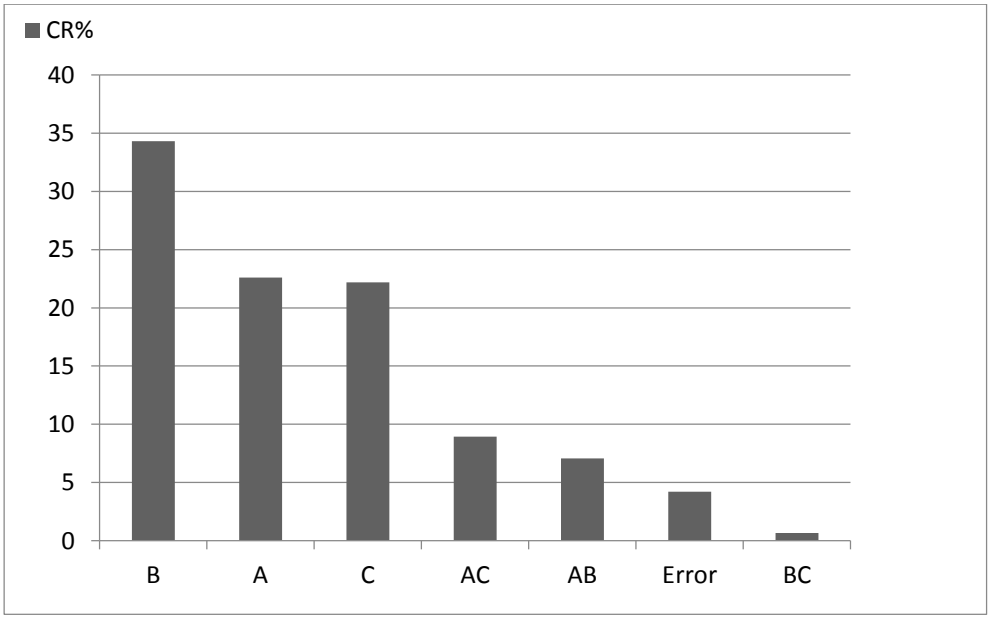

Figure 47: Pareto diagram of the main effects ranked according to decreasing contribution ratio (CR)

ANNEX III

		EOS Aluminum AlSi10Mg
Typical achievable part accuracy	*small parts*	*± 100 µm*
	large parts	
Minimum wall thickness		*0.3 ÷ 0.4 mm*
Surface roughness	*as built (cleaned)*	*Ra= 6 ÷ 10 µm* *Rz= 30 ÷ 40 µm*
	hot-peened	*Ra= 7 ÷ 10 µm* *Rz= 50 ÷ 60 µm*
Volume rate		*7.4 mm3/s*

Table 23: General and geometrical data for EOS powders

	EOS Aluminum AlSi10Mg
Material composition	*Al (balance)* *Si (9.0÷11.0 wt-%)* *Fe (≤ 0.55 wt-%)* *Cu (≤ 0.05 wt-%)* *Mn (≤ 0.45 wt-%)* *Mg (0.2÷0.45 wt-%)* *Ni (≤ 0.05 wt-%)* *Zn (≤ 0.10 wt-%)* *Pb (≤ 0.05 wt-%)* *Sn (≤ 0.05 wt-%)* *Ti (≤ 0.15 wt-%)*
Density	*2.67 g/cm^3*
Relative density	*≈ 100 %*

Table 24: Chemical and physical properties for EOS powders

		EOS Aluminum AlSi10Mg
*Tensile strength**	*XY*	*430 ± 20 MPa*
	Z	*430 ± 20 MPa*
*Yield strength (Rp 0.2 %)**	*XY*	*245 ± 10 MPa*
	Z	*220 ± 10 MPa*
Module of elasticity	*XY*	*≈ 70 ± 5 GPa*
	Z	*≈ 65 ± 5 GPa*
*Elongation at break**	*XY*	*(9.5 ± 2) %*
	Z	*(7.5 ± 2) %*
Hardness		*120 ± 5 HBW*
Fatigue strength	*Z*	*97 ± 7 MPa*

**Tensile testing according to ISO 6892-1:2009 (B) Annex D, proportional test pieces, diameter of the neck area 5 mm, original gauge length 25 mm.*

Table 25: Mechanical properties of parts produced with EOS powders (as-built)

		EOS Aluminum AlSi10Mg
Thermal conductivity (at 20°C)	*XY*	*≈ 103 ± 5 W/m°C*
	Z	*≈ 119 ± 5 W/m°C*
Specific heat capacity	*XY*	*≈ 920 ± 50 J/kg°C*
	Z	*≈ 910 ± 50 J/kg°C*

Table 26: Thermal properties of parts produced with EOS powders (as-built)

ANNEX IV

H29 data sheets

- H29 Rated torque 9.80665 N = 1 kg force - ±15 Nm
- Rated thrust – 400 N
- Maximum speed – 3000 rpm
- Power of the drive motor for rated torque values at 3000 rpm* - 5 kW
- Overload of torque and thrust permitted for a short moment Inclusive dynamic peaks - 50%
- Input resistance of the strain gauge full bridge measuring system for torque and thrust - Torque: 266 Ω Thrust: 266 Ω
- Output resistance of the strain gauge full bridge measuring system for torque thrust - Torque: 240 Ω Thrust: 240 Ω
- Temperature Compensation - With constant voltage for the supply (not for constant current)
- Recommended supply voltage for torque and thrust measurement - Up to 8 Volts
- Maximum supply voltage for torque and thrust measurement - 20 Volts
- Output voltage at rated load referring to the supply voltage for torque and thrust measurement - About 1.5mV/Volt
- Idle Torque - 0.05Nm

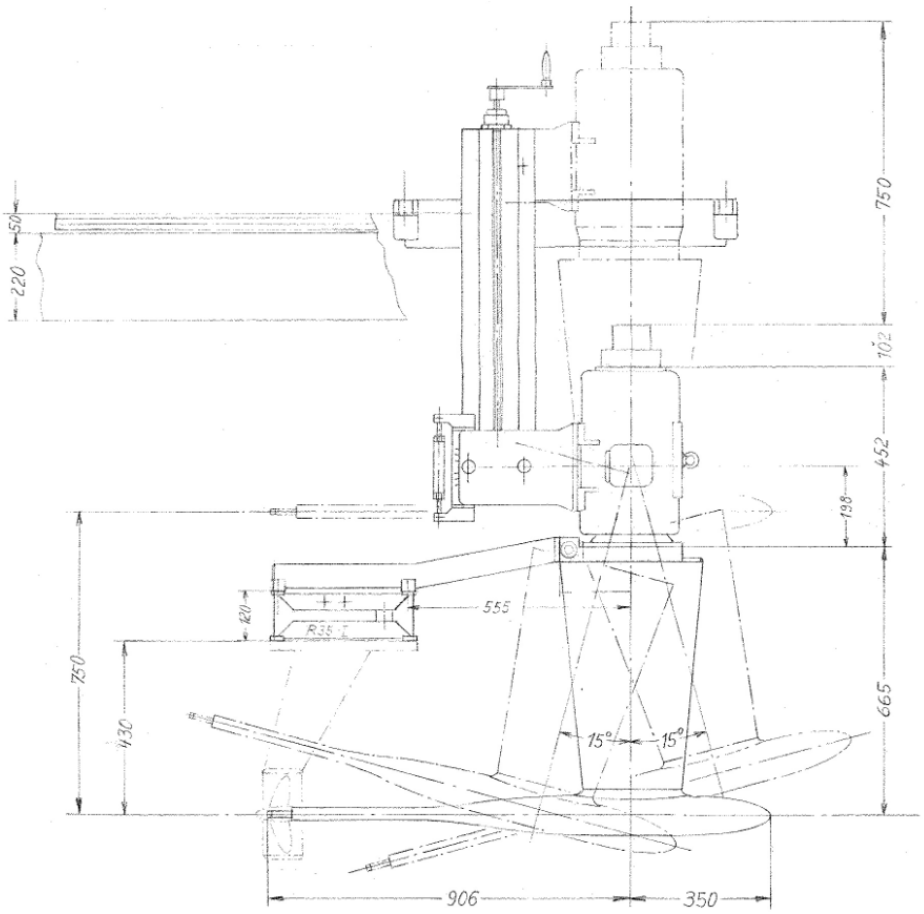

Figure 48: The Kempf & Remmers H29 propeller dynamometer

ANNEX V

In Table 27 were reported the results of towing tank experimental test for propeller printed in AlSi10Mg.

J	K_T	$10*K_Q$	η_0	V [m/s]	n [rps]
0.000	0.515	0.870	0.000	0.000	11.793
0.047	0.507	0.866	0.043	0.125	11.793
0.093	0.485	0.820	0.088	0.250	11.796
0.140	0.470	0.797	0.131	0.375	11.796
0.186	0.454	0.774	0.174	0.500	11.797
0.233	0.436	0.747	0.216	0.625	11.796
0.280	0.417	0.719	0.258	0.750	11.797
0.326	0.396	0.691	0.298	0.875	11.793
0.373	0.374	0.660	0.336	1.000	11.796
0.419	0.351	0.629	0.372	1.125	11.794
0.466	0.329	0.599	0.407	1.250	11.796
0.513	0.306	0.569	0.439	1.375	11.796
0.559	0.284	0.538	0.469	1.500	11.795
0.606	0.262	0.509	0.496	1.625	11.793
0.652	0.240	0.479	0.520	1.750	11.796
0.699	0.219	0.451	0.540	1.875	11.794
0.746	0.196	0.419	0.555	2.000	11.793
0.792	0.174	0.389	0.564	2.125	11.793
0.839	0.152	0.357	0.567	2.250	11.793
0.886	0.130	0.326	0.561	2.375	11.793
0.932	0.107	0.293	0.544	2.500	11.794
0.978	0.085	0.259	0.509	2.625	11.801
1.025	0.062	0.223	0.451	2.750	11.799
1.071	0.039	0.188	0.351	2.875	11.803
1.118	0.015	0.150	0.178	3.000	11.806
1.163	-0.009	0.112	-0.151	3.125	11.820
1.212	-0.036	0.068	-1.028	3.250	11.788

Table 27: Experimental result of towing tank test for Propeller printed in AlSi10Mg

In Table 28 were reported the results of towing tank experimental test for propeller printed in AlSi10Mg correlated to the advance coefficients J of experimental performance characteristics of the INSEAN benchmark propeller.

J	K_T	$10*K_Q$	η_0	n [rps]
0.000	0.514	0.868	0.000	11.796
0.099	0.485	0.821	0.093	11.796
0.149	0.468	0.794	0.140	11.796
0.199	0.449	0.766	0.186	11.796
0.249	0.428	0.736	0.231	11.796
0.298	0.407	0.706	0.273	11.796
0.348	0.385	0.675	0.316	11.796
0.397	0.362	0.644	0.355	11.796
0.447	0.339	0.612	0.393	11.796
0.498	0.314	0.579	0.430	11.796
0.546	0.291	0.548	0.461	11.796
0.596	0.267	0.516	0.491	11.796
0.646	0.243	0.484	0.517	11.796
0.695	0.220	0.452	0.538	11.796
0.747	0.195	0.418	0.555	11.796
0.795	0.172	0.386	0.564	11.796
0.845	0.148	0.353	0.566	11.796
0.895	0.125	0.318	0.558	11.796
0.945	0.101	0.283	0.536	11.796
0.946	0.100	0.283	0.535	11.796
0.970	0.089	0.265	0.517	11.796
0.995	0.077	0.247	0.492	11.796
1.020	0.065	0.228	0.459	11.796
1.045	0.052	0.209	0.414	11.796
1.094	0.027	0.171	0.279	11.796
1.145	0.001	0.128	0.009	11.796
1.194	-0.026	0.085	-0.591	11.796

Table 28: Experimental result of towing tank test for Propeller printed in AlSi10Mg correlated to the J of INSEAN data

In Table 29 were reported the results of towing tank experimental test for propeller printed in AlSi10Mg.

J	K_T	$10*K_Q$	η_0	V [m/s]	n [rps]
0.000	0.571	1.032	0.000	0.000	11.784
0.047	0.551	0.998	0.041	0.125	11.782
0.093	0.539	0.973	0.082	0.250	11.796
0.140	0.523	0.945	0.123	0.375	11.796
0.186	0.503	0.914	0.163	0.500	11.797
0.233	0.482	0.878	0.203	0.625	11.797
0.280	0.459	0.843	0.243	0.750	11.797
0.326	0.436	0.802	0.282	0.875	11.792
0.373	0.412	0.764	0.320	1.000	11.797
0.419	0.386	0.726	0.355	1.125	11.798
0.466	0.361	0.687	0.390	1.250	11.796
0.513	0.336	0.649	0.422	1.375	11.797
0.559	0.312	0.613	0.453	1.500	11.805
0.606	0.288	0.578	0.480	1.625	11.796
0.652	0.263	0.540	0.505	1.750	11.801
0.699	0.239	0.506	0.526	1.875	11.799
0.745	0.215	0.469	0.544	2.000	11.798
0.792	0.191	0.433	0.555	2.125	11.804
0.839	0.166	0.396	0.559	2.250	11.797
0.885	0.141	0.359	0.554	2.375	11.801
0.932	0.117	0.321	0.539	2.500	11.799
0.978	0.092	0.283	0.507	2.625	11.798
1.024	0.067	0.244	0.448	2.750	11.806
1.071	0.042	0.205	0.352	2.875	11.807
1.117	0.017	0.164	0.183	3.000	11.811
1.163	-0.010	0.122	-0.150	3.125	11.814
1.210	-0.038	0.075	-0.970	3.250	11.811

Table 29: Experimental result of towing tank test for Propeller printed in UltraT

In Table 30 were reported the results of towing tank experimental test for propeller printed in UltraT correlated to the advance coefficients J of experimental performance characteristics of the INSEAN benchmark propeller.

J	K_T	$10*K_Q$	η_0	n [rps]
0.000	0.569	1.028	0.000	11.799
0.099	0.538	0.973	0.087	11.799
0.149	0.519	0.939	0.131	11.799
0.199	0.497	0.902	0.174	11.799
0.249	0.473	0.864	0.217	11.799
0.298	0.449	0.825	0.258	11.799
0.348	0.424	0.784	0.299	11.799
0.397	0.398	0.744	0.338	11.799
0.447	0.372	0.704	0.376	11.799
0.498	0.345	0.663	0.412	11.799
0.546	0.319	0.624	0.445	11.799
0.596	0.293	0.585	0.475	11.799
0.646	0.267	0.546	0.502	11.799
0.695	0.241	0.508	0.525	11.799
0.747	0.214	0.468	0.543	11.799
0.795	0.189	0.430	0.555	11.799
0.845	0.163	0.391	0.559	11.799
0.895	0.136	0.352	0.553	11.799
0.945	0.110	0.311	0.532	11.799
0.946	0.110	0.310	0.532	11.799
0.970	0.097	0.291	0.514	11.799
0.995	0.083	0.270	0.490	11.799
1.020	0.070	0.249	0.457	11.799
1.045	0.056	0.227	0.413	11.799
1.094	0.029	0.185	0.278	11.799
1.145	0.001	0.138	0.011	11.799
1.194	-0.027	0.093	-0.562	11.799

Table 30: Experimental result of towing tank test for Propeller printed in UltraT correlated to the J of INSEAN data

In Table 31 were reported the results of towing tank experimental test for propeller printed in ABS.

J	K_T	$10*K_Q$	η_0	V [m/s]	n [rps]
0.000	0.591	1.090	0.000	0.000	11.784
0.047	0.579	1.065	0.040	0.125	11.782
0.093	0.560	1.025	0.081	0.250	11.796
0.140	0.543	0.995	0.121	0.375	11.796
0.186	0.523	0.960	0.162	0.500	11.797
0.233	0.502	0.925	0.201	0.625	11.797
0.280	0.478	0.885	0.240	0.750	11.797
0.326	0.453	0.846	0.278	0.875	11.792
0.373	0.428	0.806	0.315	1.000	11.797
0.419	0.403	0.767	0.351	1.125	11.798
0.466	0.375	0.725	0.384	1.250	11.796
0.513	0.350	0.687	0.416	1.375	11.797
0.559	0.325	0.649	0.445	1.500	11.805
0.606	0.300	0.613	0.473	1.625	11.796
0.652	0.276	0.575	0.497	1.750	11.801
0.699	0.251	0.539	0.518	1.875	11.799
0.745	0.225	0.499	0.534	2.000	11.798
0.792	0.200	0.461	0.547	2.125	11.804
0.839	0.175	0.422	0.552	2.250	11.797
0.885	0.150	0.383	0.549	2.375	11.801
0.932	0.125	0.346	0.537	2.500	11.799
0.978	0.099	0.306	0.505	2.625	11.798
1.024	0.073	0.266	0.446	2.750	11.806
1.071	0.047	0.226	0.356	2.875	11.807
1.117	0.022	0.185	0.208	3.000	11.811
1.163	-0.006	0.139	-0.081	3.125	11.814
1.210	-0.035	0.092	-0.726	3.250	11.811

Table 31: Experimental result of towing tank test for Propeller printed in ABS

In Table 32 were reported the results of towing tank experimental test for propeller printed in ABS correlated to the advance coefficients J of experimental performance characteristics of the INSEAN benchmark propeller.

J	K_T	$10*K_Q$	η_0	n [rps]
0.000	0.589	1.088	0.000	707.980
0.099	0.559	1.024	0.086	707.980
0.149	0.539	0.987	0.129	707.980
0.199	0.516	0.949	0.172	707.980
0.249	0.492	0.908	0.215	707.980
0.298	0.467	0.868	0.255	707.980
0.348	0.441	0.826	0.295	707.980
0.397	0.414	0.785	0.333	707.980
0.447	0.387	0.743	0.370	707.980
0.498	0.359	0.701	0.406	707.980
0.546	0.333	0.661	0.437	707.980
0.596	0.306	0.620	0.468	707.980
0.646	0.279	0.579	0.494	707.980
0.695	0.252	0.539	0.517	707.980
0.747	0.224	0.497	0.536	707.980
0.795	0.199	0.459	0.548	707.980
0.845	0.172	0.418	0.553	707.980
0.895	0.145	0.377	0.548	707.980
0.945	0.118	0.335	0.528	707.980
0.946	0.117	0.334	0.528	707.980
0.970	0.104	0.314	0.512	707.980
0.995	0.090	0.293	0.489	707.980
1.020	0.076	0.271	0.458	707.980
1.045	0.062	0.249	0.417	707.980
1.094	0.035	0.205	0.294	707.980
1.145	0.005	0.158	0.059	707.980
1.194	-0.024	0.110	-0.409	707.980

Table 32: Experimental result of towing tank test for Propeller printed in ABS correlated to the J of INSEAN data

RFERENCES

[1] «ASTM F2792–10 Standard Terminology for Additive Manufacturing,» in *ASTM International Committee F42 on Additive Manufacturing*, ASTM, West Conshohocken, PA, 2009,.

[2] F. Pereira, F. Salvatore, F. Di Felice and M. Soave, "Experimental Investigation of a Cavitating Propeller in," in *Proc. of the Twenty-Fifth ONR Symposium on Naval Hydrodynamics*, St. John's, Newfoundland, Canada, 2004.

[3] F. Pereira, F. Salvatore and F. Di Felice, "Measurement and Modelling of Propeller Cavitation in Uniform," *J. of Fluids Engineering,* vol. 126, no. July, p. 671–679, 2004.

[4] S. F., "The INSEAN E779A Propeller Experimental," in *Tech. Rep. D4.1.3, INSEAN, VIRTUE WP4*, May, 2007.

[5] F. Salvatore, H. Streckwall and T. van Terwisga, "Propeller Cavitation Modelling by CFD - Results from," in *First International*, Trondheim, Norway,, June, 2009.

[6] ITTC, «Testing and extrapolation methods: propulsion, performance propulsion test,» in *Tech. Rep. 7.5-02-03-01.1*, International Towing Tank Conference, 2002.

[7] ITTC, «Testing and extrapolation methods: propulsion, Propulsion, Propulsor Open Water Test,» in *Tech. Rep. 7.5-02-03-02.1*, International Towing Tank Conference, 2002.

[8] I. Gibson, D. Rosen and B. Stucker, Additive Manufacturing Technologies, Springer Ed., 2010.

[9] A. Lanzotti, D. Del Giudice, A. Lepore, G. Staiano and M. Martorelli, "On the geometric accuracy of RepRap open-source three-dimensional printer," *Journal of Mechanical Design, Transactions of the ASME,* vol. 137, 2015.

[10] A. Lanzotti, M. Grasso, G. Staiano and M. Martorelli, "The impact of process parameters on mechanical properties of parts fabricated in PLA with an open-source 3-D printer," *Rapid Prototyping Journal,* vol. 21, 2015.

[11] A. Lanzotti, M. Martorelli and G. Staiano, "Understanding process parameter effects of reprap open-source three-dimensional printers through a design of experiments approach," *Journal of Manufacturing Science and Engineering, Transactions of the ASME,* no. 137, 2015.

[12] W. E. Frazier, "Digital Manufacturing of Metallic Components: Vision," in *Solid Free Form Fabrication Proceedings*, Austin, TX, 2010.

[13] W. E. Frazier, "Metal Additive Manufacturing: A Review," *J. Mater. Eng. Perform.,* vol. 23, no. 6, p. 1917–1928, 2014.

[14] H. Ghariblu and S. Rahmati, "New Process and Machine for," *ASME J. Manuf. Sci. Eng.,,* vol. 136, no. 4, 2014.

[15] S. H. Huang, P. Liu, A. Mokasdar and L. and Hou, "Additive Manufacturing and Its Societal Impact: A Literature Review," *Int. J. Adv. Manuf. Technol.,,* vol. 67, no. (5-8), pp. 1191-1203, 2013.

[16] A. Council and M. Petch, "3D Printing: Rise of the Third Industrial Revolution," *Gyges 3D,,* p. 116, 2014.

[17] B. Berman, "3-D Printing: The New Industrial Revolution," *Bus. Horiz.,,* vol. 55, no. 2, pp. 155-162, 2012.

[18] 2. E. ISO/ASTM 52915, "Specification for Additive Manufacturing File Format (AMG) Version 1.1.".

[19] 2. E. ISO/ASTM 52921, «Terminology for Additive Manufacturing—Coordinate Systems and TestMethodologies.».

[20] R. Jones, P. S. E. Haufe, P. Iravani, V. Olliver, C. Palmer and B. A., "RepRap—The Replicating Rapid Prototyper," *Robotica,* vol. 29, no. 1, pp. 177-191, 2011.

[21] J. P. Kruth, "Material Increases Manufacturing by Rapid Prototyping," *CIRP Ann.,* vol. 40, no. 2, p. 1603–1615, 1991.

[22] G. Lart, "Comparison of Rapid Prototyping Systems," in *Proceedings of First European Conference on Rapid Prototyping*, University of Nottingham, Nottingham, UK,, 1992.

[23] N. R. Ippolito, Iuliano, L. and A. de Filippi, "A New User Part for Performance," in *Proceedings of Third European Conference on Rapid Prototyping and Manufacturing,*, University of Nottingham, Nottingham, UK, 1994.

[24] N. P. Juster and T. H. C. Childs, "“Linear and Geometric Accuracies From Layer Manufacturing,”," *CIRP Ann.,* vol. 43, no. 1, pp. 163-166, 1994.

[25] N. P. Juster and T. H. C. Childs, "A Comparison of Rapid Prototyping Processes," in *Proceedings of Third European Conference on Rapid Prototyping and Manufacturing*, University of Nottingham, Nottingham, UK, 1994.

[26] M. Shellabear, "Benchmarking Study of Accuracy and Surface Quality in RP Models," RAPTEC, Task 4.2, Report No. 2., 1999.

[27] M. Mahesh, Y. S. Wong, Fuh, Y. H. and H. T. Loh, "Benchmarking for Comparative Evaluation of RP Systems and Processes," *Rapid Prototyping J.,* vol. 10, no. 2, pp. 123-135, 2004.

[28] T. B. Sercombe and N. Hopkinson, "Process Shrinkage and Accuracy During Indirect Laser Sintering of Aluminum," *Adv. Eng. Mater.,,* vol. 8, no. 4, pp. 260-264, 2006.

[29] M. Fahad and N. Hopkinson, "A New Benchmarking Part for Evaluating the Accuracy and Repeatability of Additive Manufacturing (AM) Processes," in *2nd International Conference on Mechanical, Production and Automobile Engineering (ICMPAE 2012)*, Singapore, 2012.

[30] P. F. Jacobs, "Rapid Prototyping & Manufacturing: Fundamentals of StereoLithography," *Society of Manufacturing Engineers (SME), Dearborn, MI,* p. 434, 1992.

[31] P. F. Jacobs, "StereoLithography and other RP&M Technologies: from Rapid Prototyping to Rapid Tooling," *Society of Manufacturing Engineers (SME), Dearborn, MI,* p. 450, 1996.

[32] S. H. Park, "Robust Design and Analysis for Quality Engineering," London, UK, Chapman & Hall, 1996.

[33] M. D. C., "Design and Analysis of Experiments 5 th edition," Wiley, 1997.

[34] D. Montgomery, P. E. and V. G., in *Engineering statistic 5th ediion*, Wiley & Sons, 2011.

[35] P. J. Besl and N. D. McKay, "A Method for Registration of 3-D Shapes," *IEEE Trans. Pattern Anal. Mach. Intell.,* vol. 14, no. 2, pp. 239-256, 1992.

[36] K. M.W., J. Fuh and L. Lu, "Direct Metal Laser Sintering for rapid tooling: processing and characterization of EOS parts," *Journal of Materials Processing Technology,* 2001.

[37] S. J. A., "Materials standards for Additive Manufacturing," in *NIST – Workshop*, 2013.

[38] A. Simchi, F. Petzoldt and H. and Pohl, "On the Development of Direct Metal Laser Sintering for Rapid Tooling," *J. Mater. Process. Technol,* vol. 141, no. 3, pp. 319-328, 2003.

[39] M. W. Khaing, J. Y. H. Fuh and L. Lu, "Direct Metal Laser Sintering," *J. Mater.,* vol. 113, no. 1-3, pp. 269-272, 2001.

[40] K. Senthilkumaran, P. M. Pandey and P. V. M. Rao, "Influence of Building Strategies on the Accuracy of Parts in Selective Laser Sintering," *Mater. Des.,* vol. 30, no. 8, pp. 2946-2954, 2009.

[41] Y.-A. Song and W. Koenig, "Experimental Study of the Basic Process Mechanism for Direct Selective Laser Sintering of Low-Melting Metallic Powder," *CIRP Ann. Manuf. Technol.,* vol. 46, no. 1, pp. 127-130, 1997.

[42] J. Delgado, J. Ciurana and C. A. Rodrıguez, "Influence of Process Parameters on Part Quality and Mechanical Properties for DMLS and SLM With ron-BasedMaterials," *Int. J. Adv. Manuf. Technol.,* vol. 60, no. 5-8, pp. 601-610, 2012.

[43] M. Wong, I. Owen, C. J. Sutcliffe and A. and Puri, "Convective Heat Transfer and Pressure Losses Across Novel Heat Sinks Fabricated by Selective Laser Melting," *Int. J. Heat Mass Transfer,* vol. 52, no. 1-2, pp. 281-288, 2009.

[44] F. Calignano, D. Manfredi, E. P. Ambrosio, L. Iuliano and P. Fino, "Influence of Process Parameters on Surface Roughness of Aluminum Parts Produced by DMLS,"," *Int. J. Adv. Manuf. Technol.,* vol. 67, no. 9-12, pp. 2743-2751, 2013.

[45] N. Read, W. Wang, K. Essa and M. Attallah, "Selective laser melting of AlSi10Mg: Process optimisation and mechanical properties development," *Materials & Design,* vol. 65, pp. 417-424, 2015.

[46] G. Staiano, A. Gloria, M. Martorelli, A. Lanzotti and C. Pensa, "Experimental Study of Naval Propellers Hydrodynamic Performances to Adopt New Additive Manufacturing Processes," in *Virtual Concept International Workshop on Major Trends in Product Design*, Bordeaux (France, 2016.

[47] Zortrax, «Material Data Sheet: Z-ABS».

[48] Zortrax, «Material Data Sheet: Z-UltraT».

[49] ASTM-D3417, "Standard Test Method for Enthalpies of Fusion and Crystallization of Polymers by Differential Scanning Calorimetry (DSC)," ASTM International, West Conshohocken, PA, 1999.

[50] ASTM-D3418, "Standard Test Method for Transition Temperatures and Enthalpies of Fusion and Crystallization of Polymers by Differential Scanning Calorimetry," ASTM International, West Conshohocken, PA,, 2015.

[51] ASTM-D790, "Standard Test Methods for Flexural Properties of Unreinforced and Reinforced Plastics and Electrical Insulating Materials," ASTM International, West Conshohocken, PA, 2002.

[52] EOS, "Aluminum AlSi10Mg material datasheet".

[53] EOS, "Exposure Parameters: A short guide to Exposure Editor panel usage".

[54] S. Gerbino, D. Del Giudice, G. Staiano, A. Lanzotti and M. Martorelli, "On the influence of scanning factors on the laser scanner-based 3D inspection process," *Journal of Advanced Manufacturing Technology,* 2015.

[55] S. Gerbino, G. Staiano, A. Lanzotti and M. Martorelli, "Testing the Influence of Scanning Parameters on 3D Inspection Process with a Laser Scanner," in *Joint Conference on Mechanical, Design Engineering & Advanced Manufacturing*, Toulouse, France, 2014.

[56] M. F.R., "Two-equation eddy-viscosity turbulence models for engineering applications," *AIAA-J,* vol. 32, p. 1598–1605, 1994.

[57] F. De Luca, S. Mancini, C. Pensa and G. Staiano, "Numerical Evaluation (CFD) of Wake and Thrust Deduction Fraction of a Warped Hard Chine Hulls Systematic Series," in *the 10th International Symposium on High Speed Marine Vehicles*, Naples, IT, 2014.

[58] CD-adapco, «STAR-CCM+,» Version 9.06 UserGuide, 2015.

[59] P. Liu, N. Bose, R. Frost, G. Macfarlane, T. Lilienthal and I. Penesis, "Model Testing and Performance Comparison of Plastic and Metal Tridal Turbine Rotors," *Applied Ocean Research,* vol. 53, pp. 116-124, 2015.